A modified embedded-atom method interatomic potential for ionic systems: 2NNMEAM + Qeq

Eunkoo Lee,[1] Kwang-Ryeol Lee,[2] M. I. Baskes,[3] and Byeong-Joo Lee[1,*]

[1]*Department of Materials Science and Engineering, Pohang University of Science and Technology (POSTECH), Pohang 790-784, Republic of Korea*

[2]*Computational Science Center, Korea Institute of Science and Technology, Seoul 136-791, Republic of Korea*

[3]*Department of Aerospace Engineering, Mississippi State University, Mississippi State, Mississippi 39762, USA*

(Received 20 October 2015; revised manuscript received 14 March 2016; published 11 April 2016)

An interatomic potential model that can simultaneously describe metallic, covalent, and ionic bonding is suggested by combining the second nearest-neighbor modified embedded-atom method (2NNMEAM) and the charge equilibration (Qeq) method, as a further improvement of a series of existing models. Paying special attention to the removal of known problems found in the original Qeq model, a mathematical form for the atomic energy is newly developed, and carefully selected computational techniques are adapted for energy minimization, summation of Coulomb interaction, and charge representation. The model is applied to the Ti-O and Si-O binary systems selected as representative oxide systems for a metallic element and a covalent element. The reliability of the present 2NNMEAM + Qeq potential is evaluated by calculating the fundamental physical properties of a wide range of titanium and silicon oxides and comparing them with experimental data, density functional theory calculations, and other calculations based on (semi-)empirical potential models.

DOI: 10.1103/PhysRevB.93.144110

I. INTRODUCTION

As structural changes on an atomic scale are found to affect various materials properties or device performances, analysis of materials behavior on an atomic scale is becoming more and more important. Understanding materials phenomena on the atomic scale is rather tricky with experimental approaches but atomistic computer simulations can be an effective tool to obtain valuable information. Recently, density functional theory (DFT) calculations have been widely used to estimate materials properties such as energetics, crystal structures, elastic constants, electronic structures, etc. Though the DFT calculations have a high computational accuracy, the number of atoms that can be dealt with is limited to below 1000 atoms. Atomistic simulations based on (semi-)empirical interatomic potentials can be effectively employed to simulate structures of thousands or even millions of atoms, and can be a good companion to the DFT calculations. Important here is that the interatomic potential should be able to reproduce correctly various fundamental physical properties (structural, elastic, defect, surface, thermal properties, etc.) of relevant elements and multicomponent materials systems. With developments of interatomic potential formalisms that can cover successfully a wide range of elements and multicomponent systems, the (semi-)empirical atomistic simulation of realistic materials systems is becoming increasingly feasible.

Many empirical interatomic potential models have been proposed for various materials with ionic, metallic, or covalent bonding nature. Molecular dynamics simulations for ionic liquids were performed for the first time in the early 1970s [1,2]. The interatomic potential used for ionic liquids is the Born-Mayer-Huggins (BMH) [3] type pairwise potential that contains a Coulomb interaction term based on fixed point charges as well as a pairwise term. As crystallographic information becomes available for ionic compounds (oxides), the BMH model is upgraded so that it can describe structural properties of oxides, for example, SiO_2. The representative BMH models, TTAM [4,5] and BKS [6], fairly well describe the structural properties of various SiO_2 polymorphs, such as α-quartz, α-cristobalite, coesite, stishovite, etc. The BMH model is further modified so that it can consider electronic polarization [7], and it is finally reported that a potential based on the Morse-Stretch (MS) pairwise potential instead of the Born-Mayer type and containing a dipole polarization term performs better in describing structural properties of SiO_2 [8]. The common feature of all the above-mentioned potentials is that they are based on fixed charges, which means the variation of charge state during a reaction (oxidation, for example) cannot be investigated using atomistic simulations based on those potentials. Another problem of the potentials is that the pairwise potential (BM or MS) for the nonelectrostatic part is not suitable for description of realistic elements (silicon, for example).

It has been known that it is difficult to describe metallic or covalent elements using pairwise potentials, and it is not until the mid-1980s that many-body potentials suitable for realistic elements are proposed. The first many-body potential is the embedded-atom method (EAM) potential [9,10], which successfully describes a wide range of fundamental physical properties of metallic elements. The EAM is mainly for fcc elements, but is modified so that the potential can consider bonding directionality and thus deal with bcc, hcp, diamond-structured, and even gaseous elements. The modified EAM (MEAM [11–13]) is further modified so that it can consider up to second nearest-neighbor interactions as well as first nearest-neighbor interactions, removing some critical shortcomings found in the original version, and is named the second nearest-neighbor MEAM (2NNMEAM [14]). The 2NNMEAM model has been applied to a wide range of elements with metallic and covalent bonding nature and their alloy systems [15].

Another advancement achieved in the solid-state modeling during the same period (early mid-1980s) is the invention of the

*Corresponding author: calphad@postech.ac.kr

universal equation of state by Rose *et al.* [16–19], which states that the cohesive energy of metallic or covalent solids can be described using one mathematical expression when properly rescaled. Abell [20] shows that the MS pairwise potential can describe well the universal behavior, and Tersoff [21,22] formulates a potential model based on the MS potential introducing a bond-order term that considers many-body effects. While the basic concept of the EAM-series potentials originates from metallic bonding, the Tersoff potential is designed to describe bond breaking and new bond formation of covalent materials. The Tersoff potential is initially utilized for modeling silicon and carbon, and the formalism is extended to hydrocarbons by Brenner [23]. The Brenner potential, which is also called a reactive empirical bond-order potential (REBO), is modified for better description of hydrocarbon molecules as well as diamond, and is named the second-generation REBO (REBO2 [24]). The REBO potential has been combined with the Lennard-Jones (LJ) potential to model the van der Waals interaction, and a bond-order dependent switching function is introduced for a more realistic transition between LJ and REBO, and is named adaptive intermolecular REBO [25].

The fact that interatomic potential models have been developed separately for elements with different bonding natures (ionic, metallic, and covalent) means that atomistic simulation techniques could not be used for materials systems with complex bonding natures such as metal/metal oxides or metal/ceramic composites. Both the EAM-2NNMEAM and the Tersoff-REBO2 potentials have continuously extended the applicable materials types. Starting from metallic bonding, the MEAM is extended to covalent materials, such as silicon and carbon, and is recently further extended to saturated hydrocarbon systems [26]. On the other hand, the Tersoff-REBO2, mainly designed for covalent materials, has been continuously modified to extend its coverage to metallic systems [27,28]. However, those potentials commonly need to be further modified so that they can also consider ionic bonding.

The many-body potentials could be combined with the above-mentioned classical Coulomb interaction term based on fixed point charges. However, a more advanced extension to the ionic bonding nature becomes feasible thanks to the development of a charge equilibration (Qeq) scheme [29] that leads to equilibrium local atomic charges depending on geometry on the basis of the principle of equal chemical potential. Compared to the classical Coulomb potentials based on fixed point charges, this potential allows variation of charge state depending on the atomic environment and also considers radial distribution of electron density instead of assuming the point charge. The Qeq scheme is first combined with MS pairwise potentials (MS-Q) to describe SiO_2 [30] and Ti oxides [31,32], and is then combined with many-body potentials.

The first attempt to combine a many-body potential and Qeq scheme is made by Streitz and Mintmire [33] using the metallic EAM formalism. Zhou *et al.* [34] proposed a modified charge transfer–embedded-atom method potential, hereafter referred to as the Zhou potential, to overcome a charge instability problem and a limitation revealed when applied to metal-oxide systems of more than one metallic element, found in the original EAM + Qeq potential [33]. This potential is then applied to multicomponent metal-oxide [35] and alkali halide systems [36,37]. Recently, Lazić *et al.* [38] propose a potential for the Al-O system based on the Zhou potential in combination with a reference free version of modified EAM (RFMEAM). More recently, a combination of the Zhou potential with the MEAM is also reported [39] for an application to the Li_2MnO_3 compound.

The combination between the Tersoff potential and the Qeq scheme is first reported by Yasukawa [40] with an application to the Si/SiO_2 system. However, Sinnott, Phillpot, and co-workers [41] find that a charge instability problem inherent to the original Qeq scheme [29,33] occurs also in the Yasukawa potential and propose a modified Tersoff + Qeq potential, naming it the charge optimized many-body (COMB) potential. The COMB potential has been modified several times. The first generation COMB (COMB1) potential is for the above-mentioned Si/SiO_2 system. The COMB1 can be regarded as a slightly modified version of the Yasukawa potential to avoid the charge instability, being based on an effective point charge concept as in the original formalism. The potential is modified in a way that considers radial distribution of electron density instead of the point charge, and is applied to the Si/SiO_2 system [42] again and also to other metal/metal-oxide systems such as Hf/HfO_2 [43] and Cu/Cu_2O [44]. This potential is modified again to include charge-core charge interactions and a polarization scheme, and is applied to the Cu/Cu_2O [45] system again and to the Cu/ZnO [46] system. Most recently, the third generation COMB (COMB3), which uses terms from the latest COMB2 version [45] for electrostatic effects and from REBO2 for short-range interactions, is proposed and applied to C/H/O/N [47], U/UO_2 [48], and Ti/TiO_2 [49]. Details of the history for the COMB potential development are well summarized elsewhere [50,51].

Another many-body potential that considers variable charges in ionic bonding is the reactive force fields (ReaxFF) potential developed by van Duin *et al.* [52]. ReaxFF also uses a bond-order concept and includes Coulomb interaction, van der Waals interaction, as well as a nonelectrostatic bonding energy term, similar to the COMB potentials. ReaxFF is developed much earlier than COMB. ReaxFF is designed so that it can deal with a wide range of materials (with ionic, metallic, covalent, and even van der Waals bonding nature) from the beginning, while COMB has been continuously modified to extend its coverage. The basic concept and potential formalism of ReaxFF is much different from that of COMB even though the materials systems that can be dealt with using those potentials are now similar. For example, ReaxFF explicitly includes energy terms related to bond angle and torsion separately, while those terms are involved in the bond-order parameter in COMB. ReaxFF has been applied to hydrocarbon materials [53–58], Si-related materials [59–62], and even to metallic oxides [63–65]. More details on the comparison between ReaxFF and COMB can be found in a recent review article [50].

Three classes of the interatomic potential family—the EAM or RFMEAM + Qeq, COMB, and ReaxFF—have been briefly reviewed. One can see that the extension of the EAM or RFMEAM + Qeq potential to a wider range of materials is relatively not very active, while that for the COMB and ReaxFF is almost explosive. The difference in activity between the

EAM and bond-order potentials is partly because the type of elements (fcc metallic) dealt with using the EAM is somewhat limited compared to the bond-order potentials. However, it should be remembered that both COMB and ReaxFF are designed in a suitable form for covalent materials rather than metallic materials. Even though both potentials are being applied to metallic systems, how well those potentials perform is rarely reported for metallic alloy systems or solid-state multicomponent systems composed of metallic and covalent elements. On the other hand, the 2NNMEAM, one of the latest versions of MEAM, has been applied to a wide range of elements including bcc [66], fcc [67], hcp metals [68,69], manganese [70], and diamond-structured covalent bonding elements such as carbon [71], silicon [72], germanium [73], and their alloys. Details of the 2NNMEAM formalism and its applications are well summarized in Ref. [74].

The applicable materials classes of atomistic simulations based on semiempirical interatomic potentials would be much extended if a potential which has been successful for multicomponent alloy systems composed of metallic and covalent elements can also consider the ionic interactions. From this point of view, it is quite natural to think of the combination of the 2NNMEAM and the Qeq scheme. Such an effort has been made during the last several years, and now, the present authors, the 2NNMEAM potential developers, report a potential formalism that can cover multicomponent alloy oxides systems in a form that combines the 2NNMEAM formalism and the Qeq scheme, as a further improvement of a series of existing models [33,34,38]. An integrated solution for the technical problems [34,42,75,76] raised during the implementation of the Qeq scheme to many-body potentials, that is, the charge instability, charge for an isolated atom, and negative charge for metallic elements in alloy systems, is described in Sec. II, together with the potential formalism. We apply the potential formalism to the oxides of Ti and Si, the representative metallic and covalent element, respectively, and compare its performance with other potentials in Sec. III. Section IV is the conclusion.

II. FORMALISM OF 2NNMEAM + Qeq POTENTIAL

The formalism of the potential proposed in the present study contains two terms: nonelectrostatic and electrostatic interaction terms. The nonelectrostatic interaction term is exactly identical to the existing 2NNMEAM potential formalism and is independent from atomic charges. The electrostatic interaction term is a function of atomic positions and charges. Therefore, the total energy of the system including N atoms is expressed as

$$E^{\mathrm{Total}} = E^{\mathrm{MEAM}}(\mathbf{x}) + E^{\mathrm{ES}}(\mathbf{x},\mathbf{q}), \tag{1}$$

where $\mathbf{x} = \{\mathbf{x_1},\mathbf{x_2},\ldots,\mathbf{x_N}\}$ and $\mathbf{q} = \{q_1,q_2,\ldots,q_N\}$ is a variable set of atomic positions and charges, respectively. The nonelectrostatic and electrostatic terms are independent of each other. The 2NNMEAM energy of the reference structure basically satisfies the Rose universal equation of state (EOS) [19,77] which describes well a universal relationship between the total energy and interatomic distances in metallic and covalent solids. It is known that the Rose equation does not describe well the ionic solids. However, even in the case of ionic solids, it has been pointed out that the Rose equation is applied well if the electrostatic interaction term is considered separately [78,79]. Therefore, in the present formalism, the 2NNMEAM terms based on the Rose EOS is used without any modification and only the electrostatic term is newly introduced. Details of the 2NNMEAM formalism will not be given here. Readers are referred to Refs. [14] and [74].

The electrostatic energy is expressed by the sum of atomic energy E_i^{atom} and Coulomb pair interaction V_{ij}^{Coul}, using the terminology of Rappe and Goddard [29]:

$$E^{\mathrm{ES}} = \sum_{i}^{N} E_i^{\mathrm{atom}}(q_i) + \sum_{i,j(i\neq j)}^{N} \frac{1}{2} V_{ij}^{\mathrm{Coul}}(q_i,q_j,R_{ij}). \tag{2}$$

A. Atomic energy

Rappe and Goddard [29] expressed the atomic energy of an atom i as a quadratic polynomial of atomic charge q_i,

$$E_i^{\mathrm{atom}}(q_i) = \chi_i^0 q_i + \tfrac{1}{2} J_i^0 q_i^2. \tag{3}$$

Here, χ_i^0 is the electronegativity and J_i^0 is the atomic hardness or the self-Coulomb repulsion. It has been pointed out that this simple quadratic polynomial atomic energy term does not yield a sufficient amount of penalty energy enough to prevent atoms from being unreasonably charged beyond the charge limits. Once the atomic penalty energy fails to keep the atomic charge within a given limit, the Coulomb interaction term becomes increasingly high as cationic and anionic atoms get closer to each other. The electrostatic attractive force between the two oppositely charged ions becomes stronger and the distance between the two ions becomes even shorter as the molecular dynamics time step proceeds, and the atomic structure of the ionic crystal eventually collapses. To prevent this charge instability problem, Rappe and Goddard [29] assign limits to atomic charges and adjust the charge values whenever any equilibrium charges are calculated to go beyond the limits. In the Zhou [34] potential and COMB3 [47], the atomic energy expression is modified as in Eq. (4) and Eq. (5), respectively.

$$\begin{aligned} E_i^{\mathrm{atom}}(q_i) &= \chi_i^0 q_i + \frac{1}{2} J_i^0 q_i^2 + \omega\left(1 - \frac{q_i - q_{\mathrm{min},i}}{|q_i - q_{\mathrm{min},i}|}\right)(q_i - q_{\mathrm{min},i})^2 \\ &\quad + \omega\left(1 - \frac{q_i - q_{\mathrm{max},i}}{|q_i - q_{\mathrm{max},i}|}\right)(q_i - q_{\mathrm{max},i})^2, \end{aligned} \tag{4}$$

$$\begin{aligned} E_i^{\mathrm{atom}}(q_i) &= \chi_i^0 q_i + \tfrac{1}{2} J_i^0 q_i^2 + K_i q_i^3 + L_i q_i^4 \\ &\quad + L^{\mathrm{barr}}(q_i - q_i^{\mathrm{lim}}) q_i^4. \end{aligned} \tag{5}$$

In the Zhou potential, Eq. (4), two additional terms are added to the second-order polynomial in order to enforce the charge bounds within $[q_{\mathrm{min},i}, q_{\mathrm{max},i}]$. The COMB3, Eq. (5), uses a quartic polynomial with an additional term which is zero when q_i is within its charge limits and is assigned a rapidly increasing positive value as q_i goes beyond its charge limits.

The use of the modified atomic energy expressions removes the above-mentioned charge instability problem. However, such modifications change the numerical procedure for the

charge equilibration from a linear problem to a nonlinear problem, which makes the numerical procedure complicated and inaccurate. In the present study, the atomic energy term is defined in a way to overcome simultaneously the charge instability problem and also to keep the minimization problem linear. While the original Qeq method uses a quadratic function defined for the overall range of the charge state, in the present study, the possible charge state is divided into several ranges and a quadratic polynomial is defined for each range of the charge state. That is,

$$E_i^{\mathrm{atom}(1)}(q_i) = \tfrac{1}{2} J_i^0 q_i^2 + \chi_i^0 q_i \quad (0 < |q_i| < 1e), \tag{6a}$$

$$E_i^{\mathrm{atom}(2)}(q_i) = a_i^{(2)} q_i^2 + b_i^{(2)} q_i + c_i^{(2)} \quad (1e < |q_i| < 2e), \tag{6b}$$

$$E_i^{\mathrm{atom}(3)}(q_i) = a_i^{(3)} q_i^2 + b_i^{(3)} q_i + c_i^{(3)} \quad (2e < |q_i| < 3e), \tag{6c}$$

$$E_i^{\mathrm{atom}(4)}(q_i) = a_i^{(4)} q_i^2 + b_i^{(4)} q_i + c_i^{(4)} \quad (3e < |q_i| < 4e). \tag{6d}$$

The functional form of $E_i^{\mathrm{atom}(1)}$ is exactly the same as the atomic energy term in the original Qeq method, but its domain of definition is [0,1e]. For $|q_i|$ in the range of [1e, 2e], the atomic energy is defined by another quadratic polynomial, $E_i^{\mathrm{atom}(2)}$. This second atomic energy term is set to be smoothly continuous at $|q_i| = 1e$ with the first atomic energy term and to be larger than the first atomic energy term in the given range, [1e, 2e]. The third and fourth atomic energy terms can be defined in the same way. Namely, a quadratic spline function is used in the present study as the atomic energy term. In order to determine each quadratic uniquely, one more condition is required in addition to the continuity and smoothness. The condition is defined by introducing parameters,

$$\Delta E_i^{(n)} = E_i^{\mathrm{atom}(n)}(\pm n) - E_i^{\mathrm{atom}(n-1)}(\pm n) \quad (n = 2,\ 3,4). \tag{7}$$

Positive signs are taken for cationic elements and negative signs for anionic elements. Using $\Delta E_i^{(n)}$, the coefficients in Eqs. (6a)–(6d) can be determined recursively. That is,

$$a_i^{(n)} = a_i^{(n-1)} + \Delta E_i^{(n)}, \tag{8a}$$

$$b_i^{(n)} = b_i^{(n-1)} \mp 2(n-1)\Delta E_i^{(n)}, \tag{8b}$$

$$c_i^{(n)} = c_i^{(n-1)} + (n-1)^2 \Delta E_i^{(n)}, \tag{8c}$$

where $a_i^{(1)} = \frac{1}{2} J_i^0$, $b_i^{(1)} = \chi_i^0$, $c_i^{(1)} = 0$, and $n = 2,3,4$. By choosing positive values for $\Delta E_i^{(n)}$, the atomic energy for a higher charge state can be always larger than that for a lower charge state. The relation between atomic energy and atomic charge is illustrated in Fig. 1. $\Delta E_i^{(n)}$ ($n = 2,3,4$) are newly introduced potential parameters that prevent the charge instability and also have an effect on other properties, and are determined during the parameter optimization procedure as will be described in Sec. III A. The present approach requires an additional process to check whether computed equilibrium charges of individual cationic atoms remain in the initially assigned charge range. Details of this issue will also be described in Sec. II C.

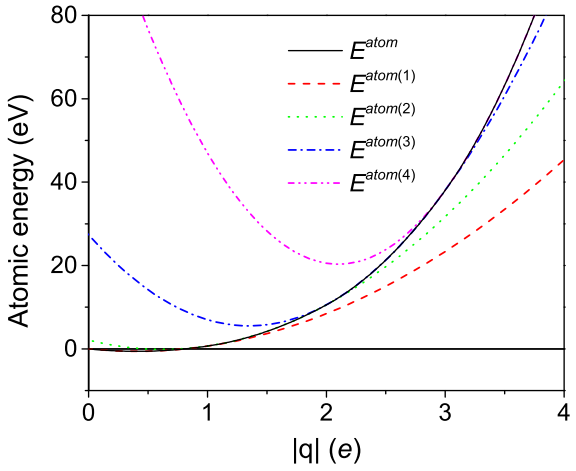

FIG. 1. Quadratic spline functions to represent the atomic energy at different charge intervals.

B. Coulomb interaction and long-range summation

In the original Qeq method [29], Coulomb interactions between two charged atoms are represented by a Coulomb integral between atomic densities of ns-Slater orbital. For large separations, the Coulomb interaction between unit charges on centers of two atoms separated by a distance R is k_c/R exactly as in the case of two point charges, where k_c is the Coulomb constant. As $R \to 0$, however, the charge distributions on the two atoms overlap and the Coulomb interaction should converge to a finite value by a shielding effect. There are a number of ways of evaluating the shielding of two charge distributions. This is related to the functional form of atomic densities or charge distributions. While Rappe and Goddard choose the ns-Slater orbital as the atomic density function, the Zhou potential and COMB3 use an atomic density function of the form

$$\rho_{(i)}(r; q_i) = Z_i \delta(r) + (q_i - Z_i) f_i(r), \tag{9}$$

which is first proposed by Streitz and Mintmire [33]. Z_i is an effective core charge and f_i the radial distribution function of the valence charge. The function $f_i(r)$ can be expressed by a simple exponential function (the density function of 1s Slater orbital):

$$f_i(r) = \frac{\zeta_i^3}{\pi} \exp(-2\zeta_i r), \tag{10}$$

where the parameter ζ_i controls the spread of the electron distribution. The Coulomb integral between two atomic densities can be written

$$V_{ij}^{\mathrm{Coul}}(q_i, q_j, R_{ij}) = k_c \iint \frac{\rho_i(r_i, q_i)\rho_j(r_j, q_j)}{|\mathbf{r}_i - \mathbf{r}_j|} d^3\mathbf{r}_i\, d^3\mathbf{r}_j. \tag{11}$$

In the present study, the atomic density function of Streitz and Mintmire, Eq. (9), is used because of its mathematical simplicity. The analytic solution of double integral in Eq. (11) is as derived by Zhou *et al.* [34].

As mentioned already, for large separations, the Coulomb interaction converges to k_c/R, which is a long-range interaction. Classically, this long-range interaction can be evaluated using the well-known Ewald summation technique [80] which

has been used in the original Qeq and Zhou potentials. The Ewald summation technique accurately computes long-range interactions. However, the computational cost is expensive due to the Fourier transform involved in the summation procedure. The COMB3 uses the charge-neutralized real-space direct summation method [81] (Wolf's direct summation method hereafter), which computes the long-range Coulomb potential without using the Fourier transform. The computational cost of Wolf's direct summation method is relatively low because the Fourier transform is not necessary. However, this method involves a probable computational error. According to Wolf *et al.* [81], the calculation for a perfect crystal can be evaluated almost accurately in comparison with Ewald summation. They report that even in the case of highly disordered systems, the amount of error is negligible. In molecular dynamic simulations, a highly efficient calculation with an acceptable amount of error is preferable to an exact calculation with an expensive computational cost. Therefore, the Wolf's direct summation [81] is used in the present study instead of the Ewald summation.

The double integral for Coulomb integration in Eq. (11) involves one long-range $1/R$ term, and the other exponential terms included are of short range. The short-range exponential terms effectively decay at relatively short distances, and therefore, can be directly summed up. The lattice summation of $1/R$ term is replaced by

$$\frac{1}{2}\sum_{i,j(i\neq j)}^{N} k_c\frac{q_iq_j}{R_{ij}} \approx \frac{1}{2}\sum_{i,j(i\neq j)}^{N} k_c q_i q_j\left(\frac{\mathrm{erfc}(\alpha R_{ij})}{R_{ij}}-\frac{\mathrm{erfc}(\alpha R_c)}{R_c}\right) - \sum_{i}^{N} k_c q_i^2\left(\frac{\mathrm{erfc}(\alpha R_c)}{2R_c}+\frac{\alpha}{\sqrt{\pi}}\right) \quad (12)$$

in the Wolf's direct summation method. Here, α is the damping coefficient and R_c is the cutoff radius. As α increases, the Coulomb potential converges at shorter cutoff radius but the error increases, and vice versa. Therefore, it is necessary to determine an optimized value of α and R_c considering computational accuracy and efficiency. By several tests, $\alpha = 0.2\,\text{Å}^{-1}$ and $R_c = 12\,\text{Å}$ are finally selected in this study.

C. Minimization method

The analytic form of the total electrostatic energy, Eq. (2), is now clearly defined as a function of atomic positions and charges. For any form of quadratic function of q_i's, one can generalize the total electrostatic energy as

$$E_{\text{total}}^{\text{ES}} = \sum_{i}^{N} q_i\chi_i + \frac{1}{2}\sum_{i,j}^{N} q_iq_jJ_{ij}, \quad (13)$$

where χ_i and J_{ij} are coefficients independent of q_i. In this study, χ_i and J_{ij} can be written

$$\chi_i = b_i^{(n)} + \sum_{j\neq i}^{N} k_c Z_j([j|f_i]-[f_i|f_j]), \quad (14)$$

$$J_{ij} = 2\left[a_i^{(n)} - k_c\left(\frac{\mathrm{erfc}(\alpha R_c)}{2R_c}+\frac{\alpha}{\sqrt{\pi}}\right)\right], \quad i=j, \quad (15a)$$

$$J_{ij} = k_c\left[[f_i|f_j]-\frac{1}{R_{ij}}+\frac{\mathrm{erfc}(\alpha R_{ij})}{R_{ij}}-\frac{\mathrm{erfc}(\alpha R_c)}{R_c}\right], \quad i\neq j, \quad (15b)$$

where $[j|f_i]$ and $[f_i|f_j]$ are Coulomb integrals [34] of two atomic densities. According to the Qeq method, the equilibrium charges can be computed by minimizing total electrostatic energy, Eq. (13), under the condition of charge conservation. This is algebraically equivalent to the electronegativity equalization saying that the chemical potentials of each atom, $\mu_i \equiv \frac{\partial E^{\text{ES}}}{\partial q_i}$, be equal to each other: $\mu_1 = \mu_2 = \cdots = \mu_N$. Therefore, the Qeq method leaves N independent equations including the charge conservation condition (usually $C = 0$ with the charge neutrality condition):

$$\sum_{i}^{N} q_i = C. \quad (16)$$

The chemical potentials, the first-order partial derivatives of E^{ES} with respect to q_i, are linear functions when the atomic energy term is quadratic. Therefore, the equations for the electronegativity equalization and the charge neutrality condition construct a linear equation system of N dimension. Rappe and Goddard solve this equation analytically by an inverse matrix method. This method can find an exact solution but can be highly inefficient for systems of large N. Moreover, the coefficient matrix is not symmetric and inverting the matrix can be further inefficient. On the other hand, the Zhou potential uses a conjugate gradient method (CGM) which finds a numerical solution of the minimization problem by an iterative algorithm.

The CGM can be more efficient than the matrix method for a large N. However, it can only be used to solve "unconstrained" optimization problems. Therefore, the equation system should be modified to an unconstrained form to be solved using the CGM method. In the case of the Zhou potential, the constraint (charge neutrality condition) is absorbed into the equations by substituting $-\sum_{i=1}^{N-1} q_i$ for q_N in Eq. (13), modifying the problem into the one with $N-1$ independent variables $q_i (i = 1, \ldots, N-1)$. Here, q_N is determined after finding the values of all the other equilibrium charges, using the relation $q_N = -\sum_{i=1}^{N-1} q_i$. However, we find that this approach can leave an unreasonable value to q_N because all numerical errors involved in the calculated $q_i (i = 1, \ldots, N-1)$ are accumulated to q_N. We also confirm during our study that the q_N can be significantly different from those for other atoms even in a perfectly ordered structure such as the NaCl structure which should satisfy $q_{\text{Na}(1)} = q_{\text{Na}(2)} = \cdots = q_{\text{Na}(N/2)} = -q_{\text{Cl}(1)} = -q_{\text{Cl}(2)} = \cdots = -q_{\text{Cl}(N/2)}$.

In COMB3, on the other hand, a dynamic fluctuating charge method proposed by Rick *et al.* [82] is used for minimizing electrostatic energy. In this approach, the charges are treated as dynamical variables that can evolve explicitly in time. The individual charges respond to deviations from the electronegativity equalization by moving toward a new charge state, which more closely satisfies the equalization condition. It can be said that this method of updating the charges is equivalent to a single-iteration steepest descent root-finding scheme [83]. Because this method does not

construct any matrix, it is computationally more efficient than the above-mentioned matrix-based methods. However, this method cannot assure the electronegativity equalization and the charge neutrality conditions, which means that the energy may not be conserved during the simulation [41,83].

Our study uses a split-charge equilibration (SQE) method proposed by Nistor *et al.* [75], which intrinsically allows the charge neutrality condition, and we use the CGM to minimize the total electrostatic energy without any constraint condition. The SQE is based on the principle of Qeq, but is different from the original Qeq in the way of representing atomic charges. This will be explained in more detail in Sec. II D and in the Appendix.

As mentioned in Sec. II A, the atomic energy term used in the present study has different expression depending on the range of q_i. Therefore, the coefficients in Eq. (13) should match atomic charges. For a given initial configuration where equilibrium charge values are not assigned to individual atoms, the atomic energy of all atoms can be given as $E_i^{\mathrm{atom}(1)}$ assuming a charge range of $[-1e,1e]$. When equilibrium charges for all atoms are computed through the energy minimization process, some atoms may have charge values beyond the initial range. The atomic energy values of those atoms are modified according to the newly computed charge. The subsequent energy minimization using the modified atomic energies may yield new values of equilibrium charges. These minimization processes should be repeated until all the equilibrium charges are in the correct domain of atomic energy. Fortunately, these processes are normally over up to three times and are required only for the initial step where the information on equilibrium charges is not available. Once equilibrium charges are assigned to individual atoms, atomic energy terms for the next step can be directly chosen from the previous ones. The equilibrium charges may change as atomic positions change. However, in ordinary molecular dynamics simulations, the atomic positions of individual atoms do not change abruptly and neither do the equilibrium charges. Therefore, the multiple energy minimization process is not required frequently during a molecular dynamics step except the first time step.

D. Charge representation

In the original Qeq, the individual atomic charges are represented by a set of q_i and they are considered as variables to be determined as a solution of an energy minimization problem. In this case, some problematic situations can occur as follows: For example, let us consider an isolated atom from a bulk. If one performs the Qeq with the given configuration, the isolated atom will get some charges even though it must be neutral due to the absence of neighboring atoms to transfer charges around. A similar situation can occur in a simulation containing two different metallic elements. In binary metallic alloys, two metallic atoms would not transfer charges to each other. However, in Qeq simulations, some charges would be given to one type of atoms from the other type of atoms as far as they have different electronegativity. These undesirable situations can be avoided if the atomic charges are generated only when there are neighbor atoms that can accept or donate electrons. Indeed, an ionic bond is formed when the valence electron density between covalently bonded atoms is concentrated on the side of a more electronegative atom.

As a means to describe the formation of ionic bonding more plausibly, Nistor *et al.* [75] propose a new scheme that allows the charge flow only between covalently bonded neighbors, using the concept of the so-called split charges. They express the charge q_i of an atom i as

$$q_i = \sum_{j}^{R_{ij}<R_{ij}^{\mathrm{bond}}} \bar{q}_{ji}, \tag{17}$$

where the split charge $\bar{q}_{ji}$ represents the charge flow from a covalently bonded neighbor atom j to atom i. R_{ij}^{bond} is the cutoff distance for defining the split charge, which is sufficiently large so that all first-neighboring atoms with opposite charges are covered. The opposite direction of charge flow is represented by the opposite sign of the split charge:

$$\bar{q}_{ij} = -\bar{q}_{ji}. \tag{18}$$

With this approach, an isolated atom remains neutral because there is no neighbor atom to transfer a charge to. If we do not define the split charge between metallic elements, no electrostatic interaction exists in purely metallic alloy systems and the systems can be described only by the nonelectrostatic term (2NNMEAM formalism, in the present case). In addition, this representation of the atomic charge always ensures charge neutrality of the whole system because the opposite direction of a split charge has a negative sign. Therefore, the CGM can be applied more straightforwardly and stably. That means that the minimization problem has a symmetric matrix and the numerical errors are not accumulated to the last q variable with no external condition. More details and some comments in using the split-charge model are described in the Appendix.

In Table I, we summarize our formalisms and techniques used for the electrostatic energy term in comparison with the original Qeq, the Zhou potential, and the COMB3. We also present the computing procedure of the electrostatic energy in the form of a flowchart in Fig. 2. The electrostatic energy is calculated at every time step. However, the electrostatic energy minimization (charge equilibration) is not performed every time step but every tens or hundreds time step, since it is a time-consuming process.

III. EVALUATION OF 2NNMEAM + Qeq FOR Ti-O AND Si-O SYSTEMS

The primary goal of our study is to develop a potential model that can simultaneously describe metallic, covalent, and ionic bonding. To demonstrate the validity of our potential model, we choose the Ti-O and Si-O systems as the representative oxide system of the metallic and covalent elements, respectively, and optimize the potential parameters for each system. We calculate fundamental physical properties (structural, elastic, thermodynamic, and defect properties) of various compounds and compare them with available experimental data or other calculations. We also examine the thermal stability of all the compounds considered and describe them in this section.

TABLE I. Summary of formalisms and techniques used for the electrostatic energy term in various potential models.

	2NNMEAM + Qeq	Original Qeq [29]	Zhou potential [34]	COMB3 [47]
Atomic energy	Quadratic spline	Quadratic	Quadratic with additional terms	Quartic with additional terms
Atomic density function in Coulomb integral	$1s$ Slater orbital with effective core charge	ns-Slater orbital	$1s$ Slater orbital with effective core charge	$1s$ Slater orbital with effective core charge
Long-range summation	Wolf's direct	Ewald	Ewald	Wolf's direct
Energy minimization subject to neutrality constraint	Solving M (the no. of bonds) linear equation of $q_i = \sum_j \bar{q}_{ji}$ using linear CGM based on split-charge equilibration	Solving N (the no. of atoms) linear equation of $\mu_1 = \mu_2 = \cdots = \mu_N$ $\sum_{i=1}^{N} q_i = 0$ with inverse matrix method	Solving $N-1$ linear equation by substituting $q_N = -\sum_{i=1}^{N-1} q_i$ using nonlinear CGM	Dynamic fluctuating charge method (extended-Lagrangian approach)

A. Parameter optimization

Our potential model, the 2NNMEAM + Qeq, has 14 MEAM parameters (E_c, R_e, α, A, $t^{(1)}$, $t^{(2)}$, $t^{(3)}$, $\beta^{(0)}$, $\beta^{(1)}$, $\beta^{(2)}$, $\beta^{(3)}$, $C_{\min}$, $C_{\max}$, and d) and seven electrostatic parameters (χ^0, J^0, $\Delta E^{(2)}$, $\Delta E^{(3)}$, $\Delta E^{(4)}$, ζ and Z) for each element. The electrostatic part of our model affects only binary properties (for titanium oxides or silicon oxides), not unary properties. This means that our 2NNMEAM + Qeq potential is equivalent to the existing 2NNMEAM potential for pure elements, and independently determined 2NNMEAM parameter sets for pure elements can be used for developing binary potentials. In this study, we use previously developed 2NNMEAM potential parameters without any modification for pure titanium [68] and silicon [72]. However, some (thermal stability) problems occur when describing the Ti-O and Si-O systems using the present pure titanium [68], silicon [72] parameters and the existing oxygen parameters [13]. The oxygen parameters are those determined by fitting a relatively insufficient amount of experimental information, the properties of O_2 dimer and O_3 trimer, while they strongly affect properties of the Ti-O and Si-O binary systems. Therefore, we modified the MEAM parameters for pure oxygen to better describe the Ti-O and Si-O binary systems by fitting the binary properties and also the properties of pure oxygen, simultaneously. The modified oxygen MEAM parameters are listed in Table II, together with parameters for pure titanium [68] and silicon [72].

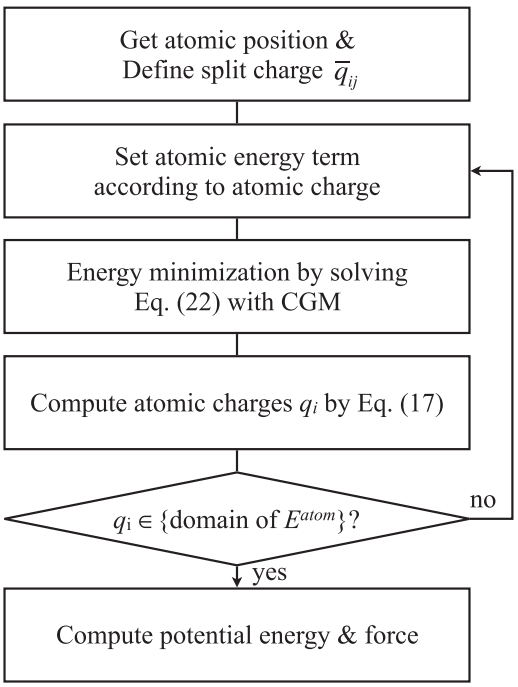

FIG. 2. The computing procedure of the electrostatic energy in the present potential formalism.

The electrostatic parameters defining the atomic energy, $\Delta E^{(3)}$ and $\Delta E^{(4)}$, are not significant in the present case because the formal charge of oxygen ($-2e$) is the upper limit of the oxygen charge, and oxide properties are well described with equilibrium charge values smaller than $2e$ for Ti and Si atoms. Nevertheless, at high-pressure or high temperature conditions, the charge values can go beyond the range $[-2e, 2e]$ and cause a charge instability problem unless $\Delta E^{(3)}$ is given a sufficiently large value. In the present study, $\Delta E^{(3)}$ is given an arbitrarily large value so that the charge of oxygen cannot be more negative than $-2e$. The effective core charge, Z, for oxygen is set to zero as has been done by Streitz and Mintmire [33] and Zhou *et al.* [34], and therefore, five parameters for titanium or silicon and four parameters for oxygen are optimized, as listed in Table II.

To describe the interaction between two different elements (i and j), the 2NNMEAM potential needs 13 more parameters, ΔE_c, R_e, α, d, $C_{\min(iji)}$, $C_{\min(jij)}$, $C_{\min(iij)}$, $C_{\min(ijj)}$, $C_{\max(iji)}$, $C_{\max(jij)}$, $C_{\max(iij)}$, $C_{\max(ijj)}$, and $\rho_0(i)/\rho_0(j)$. In the present study, only $C_{\min(\mathrm{OiO})}$ and $C_{\max(\mathrm{OiO})}$ parameters are given an adjusted value and other $C_{\min}$ and $C_{\max}$ parameters are given default assumed values, i.e., $C_{\min(i\mathrm{O}i)} = C_{\min(i)}$, $C_{\min(i i\mathrm{O})} = C_{\min(i\mathrm{OO})} = [0.5C_{\min(i)}^{1/2} + 0.5C_{\min(\mathrm{O})}^{1/2}]^2$ and $C_{\max} = 2.80$, in each binary system.

If all the unary 2NNMEAM parameter sets are available for constituent elements, the parametrization for a binary oxide system is performed over electrostatic parameters for pure elements and 2NNMEAM parameters for the binary system. In the present study, 2NNMEAM parameters for pure oxygen are also included in the parameter optimization procedure, as mentioned already. Among several candidate parameter sets for pure oxygen, a common parameter set that shows the best performance in both Si-O and Ti-O binary systems is finally selected. Since the electrostatic and 2NNMEAM parameter sets for pure oxygen are now available, the parametrization on other metal-oxide binary systems shall be performed

TABLE II. 2NNMEAM + Qeq parameters for pure Ti, Si, and O. 2NNMEAM parameters (E_c, R_e, α, A, $t^{(1)-(3)}$, $\beta^{(0)-(3)}$, $C_{\min}$, $C_{\max}$, and d) for pure Ti [68] and Si [72] are as published in literature and MEAM parameters for pure O and electrostatic parameters (χ^0, J^0, $\Delta E^{(2)-(4)}$, ζ, and Z) are optimized in the present study.

Reference structure	Ti hcp	Si Diamond	O Dimer
E_c (eV)	4.87	4.63	2.56
R_e (Å)	2.92	2.35	1.21
α	4.7195	4.9036	6.8800
A	0.66	0.58	1.44
$t^{(1)}$	6.80	1.80	0.10
$t^{(2)}$	− 2.00	5.25	0.11
$t^{(3)}$	− 12.00	− 2.61	0.00
$\beta^{(0)}$	2.70	3.55	5.47
$\beta^{(1)}$	1.00	2.50	5.30
$\beta^{(2)}$	3.00	0.00	5.18
$\beta^{(3)}$	1.00	7.50	5.57
$C_{\min}$	1.00	1.41	2.00
$C_{\max}$	1.44	2.80	2.80
D	0.00	0.00	0.00
χ^0 (eV/e)	− 1.192	− 3.17	10.11
J^0 (eV/e^2)	8.436	10.64	20.5
$\Delta E^{(2)}$ (eV)	7.97	6.14	5.63
$\Delta E^{(3)}$ (eV)	10^5[a]	10^5[a]	10^5[a]
$\Delta E^{(4)}$ (eV)			
ζ (Å^{-1})	0.83	0.48	2.39
Z (e)	1.408	0.44	0.00

[a]An arbitrary large value.

over the electrostatic parameters for the metal elements and 2NNMEAM parameters for the relevant binary systems.

Tables II and III show the finally selected potential parameters obtained by fitting physical properties (structural, elastic properties and heat of formation) of various compounds from experiments or DFT calculations, using a genetic algorithm which is a well-known global optimization method. The cutoff distance used in the 2NNMEAM calculations is 4.8 Å for both Ti-O and Si-O systems. The cutoff distance for the split charge, R_{ij}^{bond} in Eq. (17), is given a value of 2.5 Å for the Ti-O and 2.0 Å for the Si-O system, respectively, considering that the metal-oxygen distances in TiO_2 and SiO_2 polymorphs are around 2.0 and 1.6 Å, respectively.

TABLE III. 2NNMEAM parameters for the Ti-O and Si-O binary systems. i and j indicate cationic elements (Ti or Si) and oxygen, respectively.

Reference structure	Ti-O B1 (NaCl)	Si-O B3 (ZnS)
ΔE_c (eV)	1.5280	1.6400
R_e (Å)	2.0649	1.7043
α	7.4455	8.1433
d	0.01	0.03
$C_{\min(iji)}$	1.00	1.41
$C_{\min(jij)}$	0.97	0.29
$C_{\min(iij)}$	1.46	1.69
$C_{\min(ijj)}$	1.46	1.69
$C_{\max(iji)}$	2.80	2.80
$C_{\max(jij)}$	2.51	1.27
$C_{\max(iij)}$	2.80	2.80
$C_{\max(ijj)}$	2.80	2.80
ρ_0(O)/ρ_0(Ti or Si)	12.0	4.29

Before presenting the calculated properties of the Ti-O and Si-O binary systems, we present the calculated properties of pure oxygen using the modified potential parameter set listed in Table II. The MEAM potential formalism exactly reproduces the cohesive energy (E_c) and nearest distance (R_e) of the given reference structure, and there is no doubt in that the present oxygen parameters would reproduce correctly the cohesive energy and interatomic distance of the O_2 dimer. In the case of the O_3 trimer, our potential gives −2.096 eV/atom, 1.271 Å, and 116.65° for the cohesive energy, bond length, and bond angle, respectively. This calculation is comparable with the known literature value [84] of 1.28 Å for the bond length and 116.8° for the bond angle in the O_3 trimer. We also check whether our potential predicts any wrong stable phase other than O_2 dimer, by computing the cohesive energy of some artificial structures of pure oxygen such as simple cubic, fcc, bcc, hcp, and diamond structure. Those structures, except the diamond structure, are calculated to be unstable even at 0 K, while the diamond structure of pure oxygen is calculated to be metastable with a cohesive energy of −0.177 eV/atom and a nearest-neighbor distance of 1.617 Å. We finally perform a molecular dynamic simulation with a sample consisting of randomly distributed oxygen atoms to check whether some other oxygen molecules can be stabilized in addition to O_2 dimer and O_3 trimer. The molecular dynamic simulation is performed at 300 K with an N-P-T ensemble for 1 ns using a sample of 1000 atoms. We confirm that the initially liquidlike phase changes into a gaseous phase consisting mainly of O_2 dimers and some of O and O_3 molecules with an average potential energy slightly above −2.56 eV/atom, the ground state energy of the O_2 dimer. Based on the above-mentioned results, the present authors believe that the present MEAM potential for pure O describes reasonably well the properties of pure oxygen.

B. Properties of titanium oxides by the 2NNMEAM + Qeq potential

Titanium oxides have been studied with great interest industrially and academically due to their various compounds and polymorphs. Titanium dioxide (TiO_2) exists abundantly in nature as minerals such as rutile [85,86], anatase [87,88], and brookite [89,90]. In addition, metastable phases (TiO_2(B) [91], hollandite [92], ramsdellite [93]) can be synthesized experimentally. It has also been indicated from experimental and theoretical studies that there are high-pressure phases of TiO_2 such as columbite [94,95], baddeleyite [95,96], cotunnite [97], etc. In addition to the TiO_2, various compounds of titanium oxide with different stoichiometry have been reported: Magneli phases (Ti_nO_{2n-1}) [98,99], Ti_3O_5 [100,101], Ti_2O_3 [102], TiO [103,104], and so on.

An ideal interatomic potential would be the one that reproduces the structural, mechanical, and thermodynamic properties (lattice parameters, elastic constants, and heat of

TABLE IV. Lattice parameters and bulk modulus of TiO_2 polymorphs according to the present potential, in comparison with experimental data, DFT calculation, and other calculations: MS-Q, ReaxFF, and COMB3. The relative root mean squared error (rRMSE, %) of calculated lattice parameters (LP) and bulk modulus (B) with respect to available experimental data is presented in the last two rows.

		2NNMEAM + Qeq	Expt.	DFT [105]	MS-Q [32]	ReaxFF [65]	COMB3 [49]
Rutile	a (Å)	4.5761	4.5937 [85]	4.652	4.5866	4.656	4.562
	c (Å)	2.9916	2.9587 [85]	2.970	2.9581	2.998	2.967
	B (GPa)	235	212 [86]	212[a]	229		266
Anatase	a (Å)	3.8460	3.7848 [87]	3.809	3.8499	3.801	3.849
	c (Å)	9.3218	9.5214 [87]	9.732	9.0633	9.550	9.135
	B (GPa)	179	178 [88]	187[a]	176		234
Brookite	a (Å)	9.3607	9.174 [89]	9.281	9.1128	9.252	9.368
	b (Å)	5.4344	5.449 [89]	5.516	5.4497	5.487	5.424
	c (Å)	5.1441	5.149 [89]	5.185	5.1703	5.183	5.046
	B (GPa)	233	255 [90]	188[a]	211		261
TiO_2(B)	a (Å)	12.3952	12.163 [91]	12.297	12.1502		
	b (Å)	3.8281	3.735 [91]	3.764	3.8285		
	c (Å)	6.5294	6.513 [91]	6.611	6.4309		
	β (°)	107.694	107.29 [91]	106.94	107.61		
	B (GPa)	167		182[a]	184		
Hollandite	a (Å)	10.2415	10.182 [92]		9.9633		
	c (Å)	3.0361	2.966 [92]		2.9572		
	B (GPa)	98			118		
Ramsdellite	a (Å)	5.1098	4.9022 [93]	4.968	4.7210		
	b (Å)	9.3533	9.4590 [93]	9.554	9.4163		
	c (Å)	3.0295	2.9585 [93]	2.981	2.9599		
	B (GPa)	129		115[a]	138		
Columbite	a (Å)	4.6789	4.5318 [94]	4.585	4.5064	4.608	
	b (Å)	5.3631	5.5019 [94]	5.581	5.5015	5.574	
	c (Å)	4.9745	4.9063 [94]	4.935	4.9651	4.978	
	B (GPa)	197	258 [95]	204[a]	218		
Baddeleyite	a (Å)	4.8032	4.64 [96]	4.855	4.7231	4.590	
	b (Å)	4.8230	4.76 [96]	4.914	4.7440	4.892	
	c (Å)	4.9935	4.81 [96]	5.093	4.7460	4.835	
	β (°)	101.124	99.2 [96]	100.12	101.02	99.20	
	B (GPa)	238	290 [95]	149[a]	220		
Cotunnite	a (Å)	5.3188	5.163 [97]		5.1052	5.335	
	b (Å)	2.7781	2.989 [97]		2.9717	3.088	
	c (Å)	6.8323	5.966 [97]		9.0836	6.165	
	B (GPa)	275	431 [97]		92		
rRMSE of LP (%)		3.8		2.1	10.4	1.8	2.0
rRMSE of B (%)		19.9		26.5	35.1		23.4

[a]DFT values for bulk moduli are obtained in the present work by using VASP files provided in Ref. [105].

formation) of all the above-mentioned oxide phases using one set of potential parameters. We optimize the potential parameters for the Ti-O system in Tables II and III by fitting the physical properties of Ti_xO_y oxides. In this section, we compare the calculated properties of Ti_xO_y oxides with available experimental or other calculations to evaluate the quality of fitting. The defect and high-pressure properties of some TiO_2 oxides are also calculated and are compared with available information to evaluate the transferability of the potential.

Table IV compares lattice parameters and bulk modulus of various titanium dioxide (TiO_2) polymorphs calculated using the present 2NNMEAM + Qeq potential, with experimental data [85–97], DFT calculation [105], and those by three other interatomic potentials: MS-Q potential [32], reactive force field (ReaxFF) [65], and COMB3 [49]. The agreement between our calculation and experimental data is good for all polymorphs of TiO_2. The relative root mean square error (rRMSE) of our potential with respect to experimental data for lattice parameters is 3.8%. The error mostly comes from the lattice parameter c of cotunnite. It should be also noted that our potential covers a much wider range of polymorphs than the other many-body + Qeq potentials, ReaxFF and COMB3.

The elastic constants of rutile are also available. Our calculation is compared with experimental data [86], DFT [105], and other calculations [32,49] in Table V. The agreement between the present calculation and experiments or the DFT calculation is also reasonably good.

Lattice parameters and bulk modulus of various Ti_xO_y compounds (compositions other than $x{:}y = 1:2$) are

TABLE V. Elastic constants (GPa) of TiO_2 rutile according to the present 2NNMEAM + Qeq potential, in comparison with experimental data, DFT calculation, and other calculations: MS-Q, ReaxFF, and COMB3.

	2NNMEAM + Qeq	Expt. [86]	DFT[a]	MS-Q [32]	ReaxFF [49]	COMB3 [49]
C_{11}	291	268	276	294	389	318
C_{33}	447	484	469	423	484	516
C_{12}	202	175	166	202	208	257
C_{13}	170	147	147	168	151	182
C_{44}	103	124	140	96	147	123
C_{66}	204	190	212	190	201	204
rRMSE (%)	12.6		7.6	14.2	21.5	23.1

[a]DFT values for bulk modulus are obtained in the present work by using the VASP files provided in Ref. [105].

TABLE VI. Lattice parameters and bulk modulus of Ti_xO_y compounds according to the present potential, in comparison with experimental data and MS-Q calculations.

		2NNMEAM + Qeq	Expt.	DFT [105]	MS-Q [31]
Ti_6O_{11}	a (Å)	7.4679	7.517 [98]		7.436
	b (Å)	11.8159	11.986 [98]		11.82
	c (Å)	13.4827	13.397 [98]		13.30
	α (°)	98.830	98.29 [98]		98.26
	β (°)	106.415	105.52 [98]		105.8
	γ (°)	106.689	107.79 [98]		107.8
	B (GPa)	215			223
Ti_4O_7	a (Å)	5.5312	5.600 [99]		5.518
	b (Å)	7.0642	7.133 [99]		6.985
	c (Å)	12.3859	12.466 [99]		12.23
	α (°)	94.576	95.05 [99]		95.52
	β (°)	93.589	95.17 [99]		94.63
	γ (°)	109.113	108.71 [99]		108.4
	B (GPa)	211			228
$Ti_3O_5(L)$	a (Å)	9.7390	9.7568 [100]	9.810	9.433
	b (Å)	3.8276	3.8008 [100]	3.870	3.825
	c (Å)	9.1272	9.4389 [100]	9.346	9.567
	β (°)	92.262	91.547 [100]	91.15	90.26
	B (GPa)	225		180[a]	131
$Ti_3O_5(H)$	a (Å)	9.6789	9.8261 [100]	9.878	9.451
	b (Å)	3.7928	3.7894 [100]	3.803	3.782
	c (Å)	9.6165	9.9694 [100]	10.001	9.577
	β (°)	90.000	91.258 [100]	91.27	90.21
	B (GPa)	198		175[a]	226
γ-Ti_3O_5	a (Å)	9.8140	9.9701 [101]	10.218	10.26
	b (Å)	5.1296	5.0747 [101]	5.069	5.080
	c (Å)	7.0498	7.1810 [101]	7.250	6.872
	β (°)	111.974	109.865 [101]	112.04	108.3
	B (GPa)	204		177[a]	43
Ti_2O_3	a (Å)	5.1416	5.158 [102]	5.112	4.928
	c (Å)	12.6430	13.611 [102]	14.012	13.41
	B (GPa)	227		214[a]	284
α-TiO	a (Å)	7.8834	9.340 [103]	9.337	
	b (Å)	3.8995	4.142 [103]	4.173	
	c (Å)	6.5168	5.855 [103]	5.844	
	β (°)	107.77	107.53 [103]	107.32	
	B (GPa)	283		196[a]	
γ-TiO	a (Å)	3.9960	4.179 [104]	4.289	4.043
	B (GPa)	648	210 [104]	224[a]	333
rRMSE of LP (%)		4.1		1.3	2.1

[a]DFT values for bulk moduli are obtained in the present work by using the VASP files provided in Ref. [105].

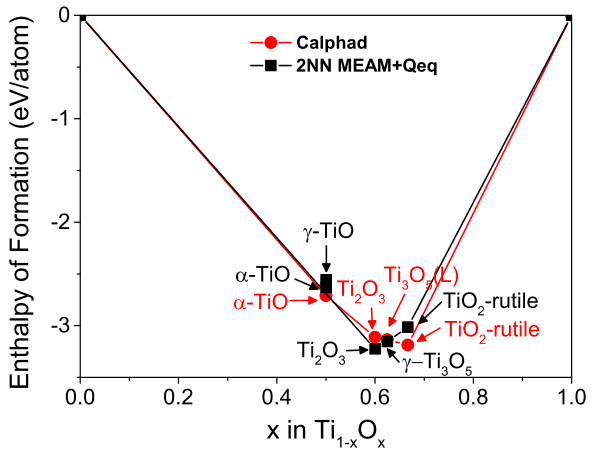

FIG. 3. Enthalpy of formation of titanium oxides according to the present 2NNMEAM + Qeq potential, in comparison with a CALPHAD calculation [106]. The reference state is hcp Ti and O_2 gas.

calculated and compared with experimental data [98–104], DFT calculation [105], and MS-Q [31] calculation (see Table VI). Here, it should be noticed that the Ti_xO_y compound phases listed in Table VI are not covered by ReaxFF [65] and COMB3 [49], and the present potential describes most of those compounds (except α-TiO and γ-TiO) even better than the MS-Q. The γ-TiO phase is known to involve vacancies [104]. However, we considered a perfect NaCl type for the γ-TiO. The agreement between our calculation and experiment data for the α-TiO and γ-TiO phases is relatively worse than that for other compound phases.

The next property examined is the thermodynamic properties of individual compounds. Figure 3 shows the calculated enthalpy of formation of the most stable oxide phase at each stoichiometric composition and at 0 K, in comparison with a CALPHAD calculation [106]. The upward curvature in the composition vs enthalpy of formation plot indicates that Ti_2O_3, Ti_3O_5, and TiO_2 are thermodynamically stable compounds, while α-TiO and γ-TiO are slightly metastable. It should be noted here that the rutile is calculated to be the most stable TiO_2 compound in agreement with experimental information [107]. However, the low temperature $Ti_3O_5(L)$ phase is calculated to be less stable than the high temperature $Ti_3O_5(H)$ phase at 0 K, according to the present potential. Actually, at the composition of Ti_3O_5, there are two stable phases, the low (L) and high (H) temperature Ti_3O_5, and a metastable γ phase. The phase stability of Ti_3O_5 polymorphs is $L > \gamma > H$ by a DFT calculation [105], while $\gamma > H > L$ by the present potential. The energy difference between γ-Ti_3O_5 and $Ti_3O_5(L)$ is not significant (about 0.039 eV/atom). Further, it should also be noted that at the composition of TiO the monoclinic α-TiO is the experimentally known [103], most stable phase at low temperatures up to 1200 K and the NaCl-type γ-TiO exists with a complicated vacancy ordering at high temperatures. However, our potential predicts α-TiO and γ-TiO as mechanically unstable phases, as will be described in more detail later on. Dilute heat of solution of oxygen in hcp and bcc Ti is −2.37 and −1.79 eV, respectively, while CALPHAD calculation [106] gives −5.65 and −5.57 eV for the same quantities. These shortcomings should be kept in mind in future applications of the present potential.

As already mentioned, rutile is the most stable phase of TiO_2. The cohesive energy of rutile and energy differences between rutile and other polymorphs, calculated by the present potential, are listed in Table VII, also in comparison with experimental data [107], the DFT calculation [105], and other calculations [49]. The cohesive energy of rutile according to our potential is −19.0317 eV/TiO_2, while it is −19.554 eV/TiO_2 according to the CALPHAD calculation [106]. Both are in good agreement with experimental value −19.9 eV/TiO_2. The DFT overestimates and the MS-Q underestimates the cohesive energy of rutile, while the ReaxFF and COMB3 yield comparable values. The energy differences between rutile and anatase or brookite according to the present potential are comparable with experimental information or other calculations.

As a means to examine the transferability of the potential, surface energy of rutile and anatase, and point defect (Schottky and Frenkel defects) formation energy of rutile are calculated and compared with first-principles data [108–112], as illustrated in Tables VIII and IX, respectively. Here, all calculations are for relaxed structures. In the case of (100) and (110) surface of rutile, there are two possible terminations (Ti terminated and O terminated). The representative, O-terminated surface is considered in the present calculation. Other surfaces are uniquely defined. For the point defects, two types of relative position of defects are considered, where point defects (Ti

TABLE VII. Cohesive energy of rutile and energy differences between rutile and other TiO_2 polymorphs, calculated using the present 2NNMEAM + Qeq potential, in comparison with experimental data, DFT calculations, and other calculations: MS-Q, ReaxFF, and COMB3.

			$\Delta E_{\text{rutile}\to\text{phase}}$ (eV/TiO_2)			
Phase	2NNMEAM + Qeq	Expt. [107]	DFT [105]	MS-Q [49]	ReaxFF [49]	COMB3 [49]
Rutile	− 19.0317	− 19.900	− 26.810	− 8.248	− 21.225	− 19.189
Anatase	+0.0458	+0.035	− 0.093	+0.057	+0.034	+0.129
brookite	+0.0300	+0.008	− 0.051	+0.037	+0.144	+0.080
TiO_2(B)	+0.1585		− 0.111			
Hollandite	+0.0973			+0.386		+0.275
Ramsdellite	+0.1404		+0.066	+0.130		+0.263
Columbite	+0.0537		− 0.018	+0.074		+0.010
Baddeleyite	+0.1456		+0.084	+0.515		+0.667
Cotunnite	+0.6297			+0.553		+0.739

TABLE VIII. Calculated surface energy (J/m^2) of rutile and anatase, in comparison with first-principles data [108–110]. There are two possible terminations (Ti terminated and O terminated) for (100) and (110) surfaces of rutile. The representative surface (and thus considered here) is the O terminated. Other surfaces are uniquely defined.

	Surface	2NNMEAM + Qeq	DFT
Rutile	(001)	1.18	1.36 [108], 1.68 [109]
	(100)	0.93	0.68 [108], 1.04 [109]
	(110)	0.61	0.48 [108], 0.86 [109], 0.31 [110], 0.84 [110]
Anatase	(001)	0.63	0.90 [110], 1.38 [110]
	(100)	0.75	0.53 [110], 0.96 [110]
	(101)	0.61	0.44 [110], 0.84 [110]

vacancy and two O vacancies for Schottky, Ti vacancy and Ti interstitial for cation Frenkel, and O vacancy and O interstitial for anion Frenkel) are neighboring or distanced and noninteracting. It is shown that our calculation is comparable with available first-principles data for both the surface energy and defect formation energy.

We also investigate the structural changes (lattice parameter a and c, and volume) of rutile and anatase at high pressures and compare them with experimental information [113,114] in Fig. 4. It is clear that our potential describes well the high-pressure properties even though those properties are not included in the fitting procedure.

The last quantity investigated for the Ti-O system is the charge state of each element in individual compound phases. The charge equilibration scheme enables the computation of variable charges depending on local environments, and the average charge of titanium and oxygen atoms in individual titanium oxide phases is different as listed in Table X. According to our potential, the average charge of Ti in the three TiO_2 polymorphs—rutile, anatase, and brookite—is $+1.408e$,$+1.409e$, and $+1.408e$, respectively, while a DFT calculation [49] gives $+2.26e$ and $+2.24e$ for rutile and anatase, respectively. COMB3 [49] gives $+1.91e$, $+1.88e$, and $+1.89e$ for rutile, anatase, and brookite, respectively, while other potentials have smaller values (ReaxFF [49]: $+1.60e$, $+1.58e$, and $+1.58e$; MS-Q [32]: $+1.15e$, $+1.12e$, and $1.14e$). It should be emphasized here that it is difficult to obtain information about the charge state of individual atoms in solids by experiments, and the charge is not a well-defined quantity even in DFT calculations. The average charge of Ti in other compound phases is calculated to decrease with a decreasing O/Ti ratio, as can be well expected.

TABLE IX. Calculated Schottky (S), cation Frenkel (CF), and anion Frenkel (AF) formation energy (eV) of rutile, in comparison with first-principles data [111,112]. Two types of relative position of point defects are considered, where point defects (Ti vacancy and two O vacancies for Schottky, Ti vacancy and Ti interstitial for cation Frenkel, and O vacancy and O interstitial for anion Frenkel) are neighboring or distanced and noninteracting.

Defect	2NNMEAM + Qeq	DFT
$S_{Neighboring}$	3.62	3.01 [111]
$S_{Noninteracting}$	5.97	5.47 [111], 4.03–6.55 [112]
$CF_{Neighboring}$	4.87	1.98 [111]
$CF_{Noninteracting}$	6.63	3.84 [111], 3.07–5.46 [112]
$AF_{Neighboring}$	2.54	
$AF_{Noninteracting}$	4.00	

C. Properties of silicon dioxides by the 2NNMEAM + Qeq potential

Different from the Ti-O binary system, the Si-O system has only one compound, the silicon dioxide (SiO_2), on the phase diagram. However, the SiO_2 is characterized by the existence of a large number of polymorphs. Among the polymorphs, quartz (α- [115] and β- [116]), β-tridymite [117], and cristoballite (α- [118] and β- [119]) appear as thermodynamically stable phases at different temperature ranges. Coesite [120] is a high-pressure polymorph of SiO_2 with a rather complex monoclinic structure. Keatite [121] is found in nature, although rarely, and is mainly synthesized by crystallization at moderate temperature (473–673 K) and pressure (2–3 kbar). Stishovite [122] (an isomorph with rutile TiO_2) is also synthesized at high-pressure conditions. The issue here is to reproduce the fundamental physical properties of all the above-mentioned SiO_2 polymorphs using one set of potential parameters, as has been done for the Ti-O system.

The structure of α-quartz may be considered as a distorted form of the idealized structure of β-quartz, and the β-cristobalite and β-tridymite structures can be idealized by choosing some structural parameters to be more symmetric (idealized β-cristobalite and β-tridymite are represented with a prefix "i-": i-cristobalite and i-tridymite, respectively). Our potential can reasonably reproduce these minimal structural differences in low symmetric and idealized structures. Table XI shows the calculated lattice parameters and bulk modulus of SiO_2 polymorphs, in comparison with experimental data [115–122], DFT calculations [123], and other calculations [4–6,30,42,124] using (semi-)empirical potentials. Most of our calculation results are in good agreement with experimental data or DFT calculations. Experimental information on elastic constants of two SiO_2 polymorphs, α-quartz [125] and α-cristobalite [126], is available and compared with the present calculation and other calculations [6,42,127] in Table XII. Clearly, the classical pairwise fixed-charge potentials (BKS [6,127] and TTAM [127]) reproduce the elastic constants better than the recently developed potentials based on many-body and charge equilibration schemes (the present one and COMB2 [42]), probably because of the smaller number of properties considered during parameter fitting.

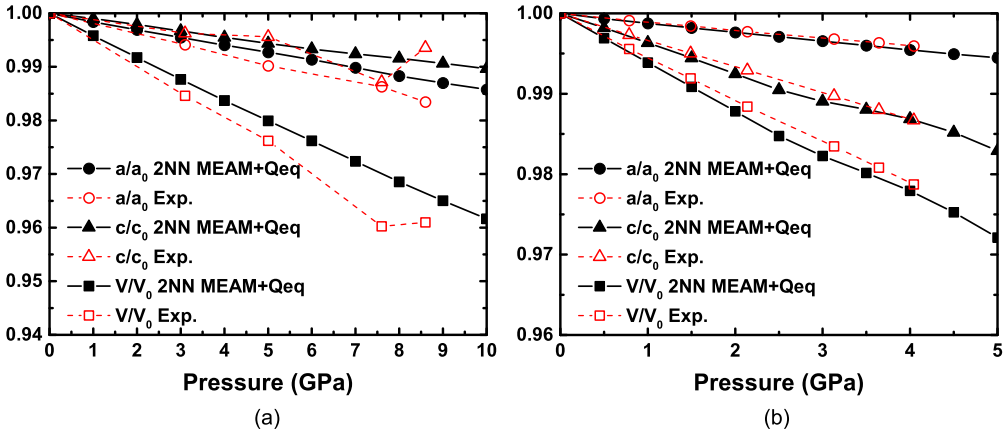

FIG. 4. Calculated pressure-induced structural changes in (a) rutile and (b) anatase, in comparison with experimental data [113,114].

Most SiO_2 structures are composed of corner-sharing tetrahedral SiO_4 units. The structures are similar to each other and only differ in the connectivity of the basic tetrahedral units and hence show only minimal structural energy differences [123]. It is well known that α-quartz is the most stable structure among SiO_2 polymorphs. Hence, we calculated the cohesive energy of α-quartz and energy differences between α-quartz and other polymorphs, and compared them with experimental data [128,129], DFT calculation [123], and other calculations [5,42] as shown in Table XIII. The calculated cohesive energy of α-quartz is $-20.0043\,\mathrm{eV/SiO_2}$, close to the experimental value $-19.23\,\mathrm{eV/SiO_2}$, and the energy differences between α-quartz and other polymorphs according to our potential are in reasonable agreement with experimental data and/or DFT calculation except for stishovite. Stishovite has octahedral SiO_6 basic unit in contrast to other polymorphs. This structural difference of stishovite makes a noticeable energy difference compared to other polymorphs, as shown in our calculation as well as in the DFT and COMB2 calculations.

TABLE X. Average charges (e) of Ti and O atoms in individual titanium oxide phases according to the present 2NNMEAM + Qeq potential.

Phase	Ti	O
TiO_2-rutile	+1.408	−0.704
TiO_2-anatase	+1.409	−0.705
TiO_2-brookite	+1.408	−0.703
TiO_2(B)	+1.405	−0.703
TiO_2-hollandite	+1.405	−0.702
TiO_2-ramsdellite	+1.403	−0.702
TiO_2-columbite	+1.407	−0.703
TiO_2-baddeleyite	+1.405	−0.702
TiO_2-cotunnite	+1.391	−0.695
Ti_6O_{11}	+1.378	−0.752
Ti_4O_7	+1.364	−0.779
$Ti_3O_5(L)$	+1.355	−0.813
Ti_3O_5 (H)	+1.362	−0.817
γ-Ti_3O_5	+1.349	−0.809
Ti_2O_3	+1.314	−0.876
α-TiO	+1.076	−1.076
γ-TiO	+1.121	−1.121

However, it should be noted that the energy difference by our calculation is much larger than other calculations.

As mentioned already, the phase diagram of the Si-O binary system shows that only SiO_2 compounds exist in the whole compositional range. This means that no other compound with different stoichiometric compositions should exist as a stable compound on the composition vs enthalpy of formation plot at 0 K. To confirm this, we calculate the enthalpy of formation of artificial SiO compound phases (NaCl-type B1, CsCl-type B2, and ZnS-type B3 structure) and check whether our potential reproduces these compound phases as meta or unstable phases. Figure 5 shows calculated enthalpy of formation of B1, B2, and B3 SiO and stable SiO_2 phases at 0 K. The data points for B1, B2, and B3 are all above the line connecting pure Si and stable SiO_2, which means that B1, B2, and B3 SiO phases are not stable according to the present potential.

The (0001) surface energy values are available [130] for α-quartz from first principles, and a comparison is made with the present calculation (Table XIV) to examine the transferability of the potential. It should be mentioned here that the simulation sample for the (0001) surface has two surfaces, one at the top and the other at the bottom of the sample. One is Si terminated, while the other is O terminated. According to our potential, the Si-terminated surface is unstable (the outmost Si layer tends to change its position with the O layer). The present calculation for the Si/O-terminated surface is carried out for the unrelaxed structure, while calculations for the other surfaces and point defects are for relaxed structures. The cleaved surface is the O-terminated surface without reconstruction. Our potential generally underestimates the surface energy of α-quartz and fails to reproduce the reconstruction on the (0001) surface. The information on the defect formation energy is not available even for the α-quartz, except the first-principles value [131] for anion Frenkel defect in noninteracting condition. Similar calculations of point defect formation energy are carried out as in the rutile for future comparisons, and the results are presented in Table XV.

Pressure-induced structural changes of SiO_2 polymorphs (α-quartz, α-cristobalite, and stishovite) are investigated as presented in Fig. 6, in comparison with experimental data [115,118,122]. Our potential overestimates the effect of pressure on the lattice parameters and volume of α-quartz,

TABLE XI. Lattice parameters and bulk modulus of SiO_2 polymorphs according to the present 2NNMEAM + Qeq potential, in comparison with experimental data, DFT calculation, and other potentials, COMB2, MEAM, MS-Q, BKS, and TTAM (Q: quartz; C: cristobalite; T: tridymite). The rRMSE (%) of calculated lattice parameters (LP) and bulk modulus (B) with respect to available experimental data is presented in the last two rows.

		2NNMEAM + Qeq	Expt.	DFT [123]	COMB2 [42]	MEAM [124]	MS-Q [30]	BKS [6]	TTAM [4,5]
α-Q	a (Å)	5.0446	4.916 [115]	4.8992	4.856	4.780	4.9796	4.941	5.02
	c (Å)	5.4662	5.4054 [115]	5.3832	5.316	5.258	5.4268	5.449	5.53
	B (GPa)	35	37 [115]	35	64	35		41	39
β-Q	a (Å)	5.1073	4.9977 [116]	5.0261		5.000	5.1195		5.17
	c (Å)	5.5689	5.4601 [116]	5.5124		5.459	5.4353		5.73
	B (GPa)	149		133		233			134
α-C	a (Å)	4.9663	4.972 [118]	4.9751	4.98	4.570	4.9336	4.890 [124]	4.96
	c (Å)	6.5652	6.922 [118]	6.9261	6.94	6.535	6.4706	6.530 [124]	6.68
	B (GPa)	12	12 [118]	13	17	17		24 [124]	20
β-C	a (Å)	7.0088	7.159 [119]	7.13			6.9093		7.07
	B (GPa)	15	16 [119]	14					19
i-C	a (Å)	7.4540		7.352		7.360			
	B (GPa)	174		129		123			
β-T	a (Å)	8.7254	8.74 [117]	8.9766					
	b (Å)	4.9121	5.04 [117]	5.0084					
	c (Å)	8.3730	8.24 [117]	8.1786					
	B (GPa)	32		31					
i-T	a (Å)	5.2700		5.1908		5.16	5.0101		5.37
	c (Å)	8.6038		8.4702		8.43	8.1391		8.75
	B (GPa)	174		140		139			138
Coesite	a (Å)	7.2750	7.1356 [120]	7.0672			7.2077		7.23
	b (Å)	12.4905	12.3692 [120]	12.2907			12.5370		12.74
	c (Å)	7.3033	7.1736 [120]	7.1406			7.2646		7.43
	β (°)	120.688	120.34 [120]	120.416			120.13		120.8
	B (GPa)	94	96 [120]	94					108
Keatite	a (Å)	7.5698	7.464 [121]	7.4669			7.5462		
	c (Å)	8.9700	8.620 [121]	8.5639			8.2529		
	B (GPa)	65		52					
Stishovite	a (Å)	4.1818	4.1797 [122]	4.1636			4.2382		4.26
	c (Å)	2.5992	2.6669 [122]	2.6696			2.6154		2.75
	B (GPa)	322	313 [122]	293					299
rRMSE of LP (%)		2.2		0.8	1.0	4.3	2.4	3.0	2.7
rRMSE of B (%)		4.0		7.8	59.4	29.7		71.1	31.6

while describing well the same properties of α-cristobalite and stishovite.

We also calculate the average charges of Si and O atoms in SiO_2 polymorphs, as listed in Table XVI. As mentioned already, most SiO_2 structures consist of SiO_4 basic tetrahedral units, except stishovite of which the basic unit is the SiO_6 octahedral. Thus, we can notice that the average charges of Si in most SiO_2 polymorphs have similar values, around

TABLE XII. Elastic constants (GPa) of SiO_2 α-quartz and α-cristobalite according to the present 2NNMEAM + Qeq potential, in comparison with experimental data and other potentials, COMB2, BKS, and TTAM.

	α-quartz					α-cristobalite				
	2NNMEAM+ Qeq	Expt. [125]	COMB2 [42]	BKS [6]	TTAM [6]	2NNMEAM+ Qeq	Expt. [126].	COMB2 [42]	BKS [127]	TTAM [127]
C_{11}	97	87	99	91	72	38	59	137	65	48
C_{33}	64	106	111	107	91	51	42	118	38	35
C_{12}	15	7	5	8	9	10	4	18	7	6
C_{13}	9	12	38	15	12	− 10	− 4	43	− 1	− 4
C_{44}	37	58	42	50	40	47	67	55	70	58
C_{66}	41	40	47	41	32	24	26	29	28	20
rRMSE	52.8		90.4	13.2	21.1	89.1		508.9	43.8	25.3

TABLE XIII. Cohesive energy of α-quartz and the energy differences between α-quartz and other SiO_2 polymorphs calculated according to the present 2NNMEAM + Qeq potential, in comparison with experimental data, DFT calculations, and other calculations, COMB2 and TTAM.

	$\Delta E_{\alpha-\text{quartz}\rightarrow\text{phase}}$ (eV/SiO_2)				
Phase	2NNMEAM + Qeq	Expt. [128,129]	DFT [123]	COMB2 [42]	TTAM [5]
α-quartz	− 20.0043	− 19.23	− 25.964	− 20.63	− 22.2
β-quartz	+0.001	+0.051	+0.026	+0.108	+0.063
α-cristobalite	+0.002	+0.030	+0.025	+0.049	+0.188
β-cristobalite	+0.010	+0.054	+0.033		+0.212
i-cristobalite	+0.028		+0.061	+0.500	
β-tridymite	+0.016		+0.034	+0.635	
i-tridymite	+0.032		+0.045		+0.259
Coesite	+0.040	+0.030	+0.012	+0.082	
Keatite	+0.001		+0.022		
Stishovite	+3.451		+0.105	+1.196	+0.048

+1.2e. Those values are comparable with the average charge of Si in α-quartz from MS-Q (+1.32e) [30] and ReaxFF (+1.35e) [59], while COMB2 [42] yields a larger value, +2.92e. BKS [6] and TTAM [4,5] use an effective fixed charge, +2.4e, for all Si atoms and −1.2e for all O atoms in SiO_2 polymorphs.

D. Thermal stability and thermal properties

All the properties calculated in previous sections are 0 K properties. According to our experience, so many potentials that perform well at 0 K often fail at finite temperatures. The representative example of the failure is a transformation of the structure into an unknown structure, which decreases the energy to a level that makes the unknown structure a stable phase on the phase diagram. In this case, we cannot use the potential for finite temperature simulations.

To check the performance of our potentials at finite temperatures, we examine the energy and structural changes of all the compound phases considered, during heating. The initial structures of individual compound phases relaxed at 0 K are heated to 3000 K, increasing the temperature by 200 K and equilibrating the structures (containing 2000-4000 atoms) using a molecular dynamics simulation for 10 picoseconds at each temperature with an N-P-T ensemble. Then, the heated structures at each temperature are rapidly cooled to 0 K to see whether the initial 0 K structures have recovered. If the potentials perform correctly, one can expect that the internal energy of individual phases would monotonically increase with an increasing temperature and abruptly change when a transformation to a more stable, known structure or melting occurs. The point to look for during the heating is whether any compound phase transforms to an unknown structure, decreasing the energy and thus making itself the most stable phase at the corresponding composition. By confirming the recovery of initial (0 K) structure after rapid cooling from finite temperatures, we want to confirm that the potential does not generate undesirable structures during dynamic simulations (at finite temperatures) and can be used for dynamic simulations in the whole temperature range. Thermal properties such as the thermal expansion coefficient and heat capacity are also calculated from this heating simulation.

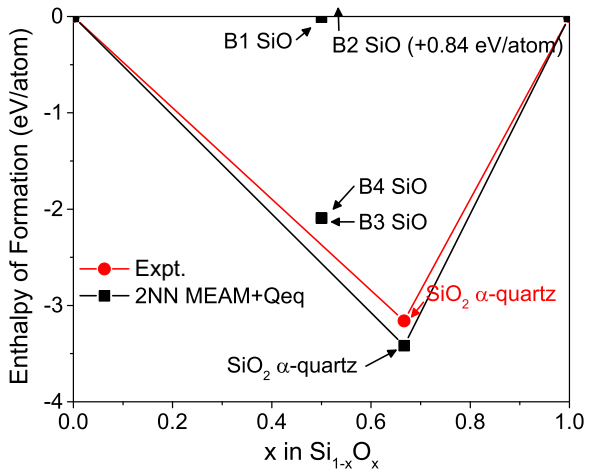

FIG. 5. Enthalpy of formation of silicon oxides according to the present 2NNMEAM + Qeq potential, in comparison with experimental data [129]. The reference state is diamond Si and O_2 gas.

Figure 7(a) shows the change of internal energy of TiO_2 polymorphs with an increasing temperature, and Fig. 7(b) shows the internal energy of individual structures rapidly cooled from each heating temperature to 0 K. All the TiO_2 polymorphs show monotonic increases of internal energy with temperature and all the polymorphs except cotunnite recover the initial 0 K energy when rapidly cooled to 0 K from temperatures below melting temperature. According to the present potential, the cotunnite transforms to another

TABLE XIV. Calculated (0001) surface energy (J/m^2) of α-quartz in comparison with first-principles data [130]. The Si-terminated surface is unstable. The calculation is carried out for an unrelaxed structure with a Si-terminated and an O-terminated surface in each side of the sample. The cleaved surface is O-terminated surface without reconstruction.

Surface	2NNMEAM + Qeq	DFT [130]
Si/O terminated	1.39	3.42
Cleaved	0.65	2.23
Reconstructed		0.39

TABLE XV. Calculated Schottky (S), cation Frenkel (CF), and anion Frenkel (AF) formation energy (eV) of α-quartz, in comparison with first-principles data [131]. Two types of relative position of point defects are considered, where point defects (Si vacancy and two O vacancies for Schottky, Si vacancy and Si interstitial for cation Frenkel, and O vacancy and O interstitial for anion Frenkel) are neighboring or distanced and noninteracting.

Defect	2NNMEAM + Qeq	DFT [131]
$S_{Neighboring}$	2.49	
$S_{Noninteracting}$	1.63	
$CF_{Neighboring}$	2.50	
$CF_{Noninteracting}$	4.94	
$AF_{Neighboring}$	1.52	
$AF_{Noninteracting}$	4.72	7.0

structure with a slightly different lattice parameter c during heating. However, the transformed structure remains as a structure with the highest energy among the TiO_2 polymorphs considered. The slope of internal energy vs temperature curves corresponds to the specific heat. All the TiO_2 polymorphs yield a similar value of specific heat, around 77 J/mole K, with the present potential, while the experimental value [132] is 55.06 and 55.52 J/mole K for rutile and anatase, respectively. The volumetric thermal expansion coefficient is calculated to be 2.0×10^{-5}, 2.7×10^{-5}, and $2.3 \times 10^{-5}\,K^{-1}$ for rutile, anatase, and brookite, respectively, which is comparable with experimental values, 2.46×10^{-5} and $1.45 \times 10^{-5}\,K^{-1}$ for rutile [132] and anatase [87], respectively.

In a way similar to the TiO_2 polymorphs, we examine the change in internal energy of other Ti_xO_y compound phases as shown in Figs. 7(c) and 7(d). All the compounds except α- and γ-TiO show a monotonic increase of internal energy with an increasing temperature before melting and recover the initial 0 K energy when rapidly cooled to 0 K. However, as mentioned in Sec. III B, α- and γ-TiO are mechanically unstable, that is, they do not maintain the crystalline structure at finite temperatures but transform to amorphous phases with an energy drop. The enthalpy of amorphous TiO at 0 K is below the line that connects the enthalpy of formation of pure Ti and Ti_2O_3 in the enthalpy of formation vs composition plot (Fig. 3) by about 0.1 eV/atom. Even though the 0.1 eV/atom is a small amount compared to the enthalpy of formation values of Ti oxides (around 3 eV/atom), we must pay attention to the structural stability when using the present potential for a molecular dynamics simulation near the equiatomic composition ($x_O = 0.5$) of the Ti-O binary system.

TABLE XVI. Average charges (e) of Si and O in SiO_2 polymorphs according to the present 2NNMEAM + Qeq potential.

Phase	Si	O
α-quartz	+1.204	−0.602
β-quartz	+1.201	−0.601
α-cristobalite	+1.204	−0.602
β-cristobalite	+1.199	−0.600
i-cristobalite	+1.186	−0.593
β-tridymite	+1.196	−0.598
i-tridymite	+1.186	−0.593
Coesite	+1.210	−0.605
Keatite	+1.200	−0.600
Stishovite	+1.224	−0.612

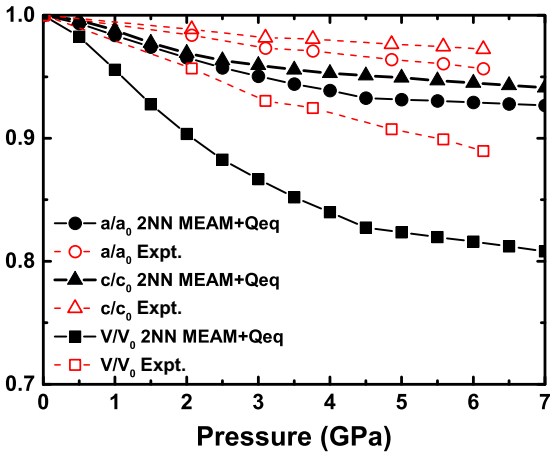

(a)

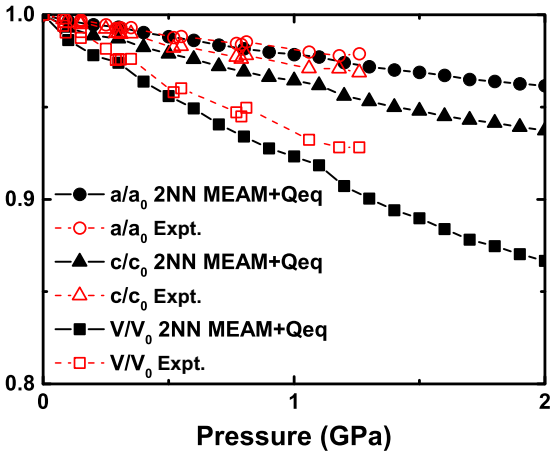

(b)

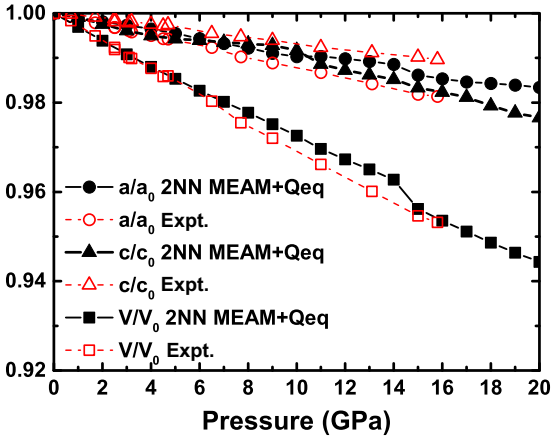

(c)

FIG. 6. Calculated pressure-induced structural changes in (a) α-quartz, (b) α-cristobalite, and (c) stishovite, in comparison with experimental data [115,118,122].

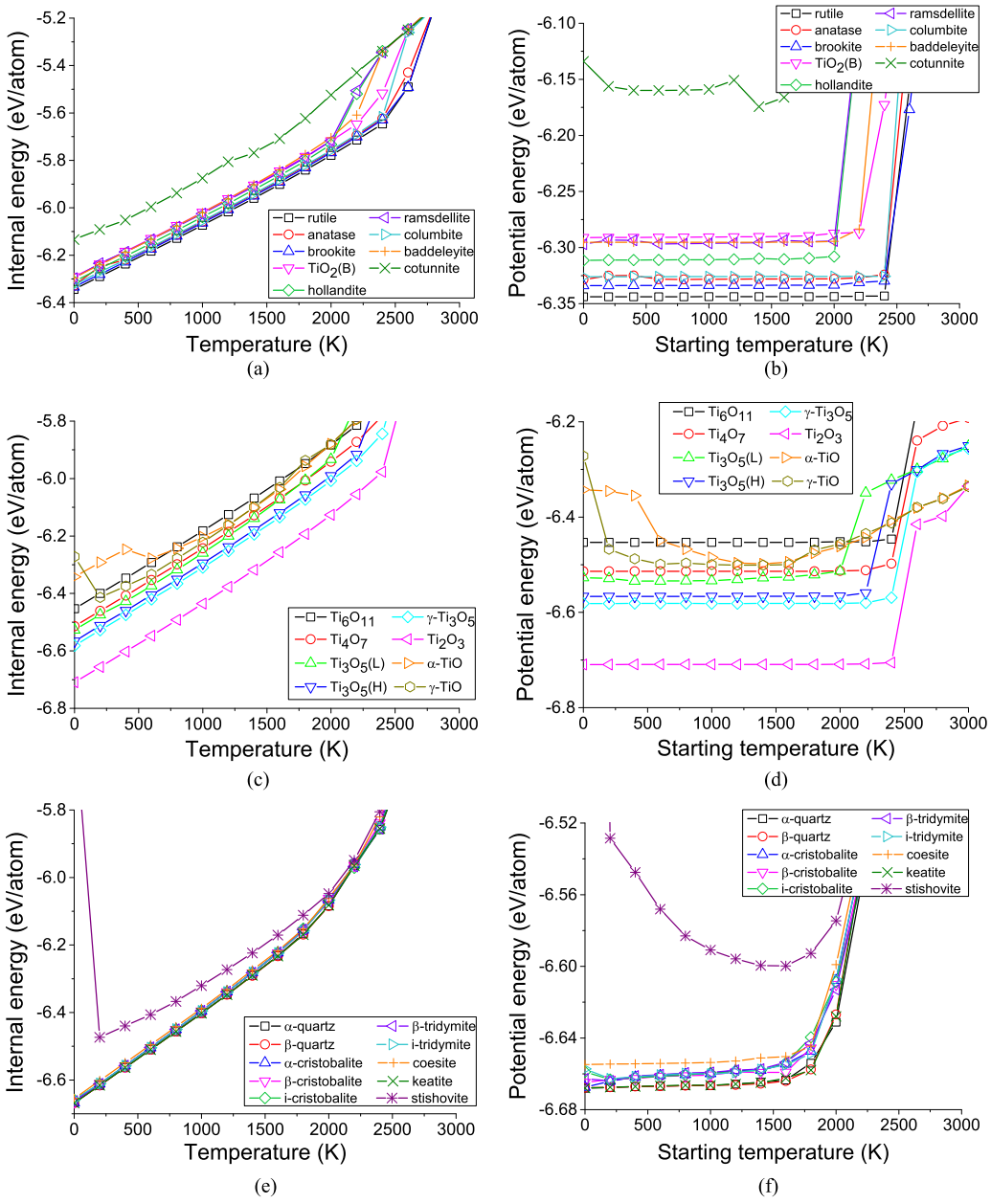

FIG. 7. Change of internal energy of [(a), (b)] TiO_2 polymorphs, [(c), (d)] Ti_xO_y compounds, and [(e), (f)] SiO_2 polymorphs with [(a), (c), (e)] increasing temperature and [(b), (d), (f)] after rapid cooling to 0 K from each temperature.

Figures 7(e) and 7(f) show the change of internal energy for SiO_2 polymorphs during heating and after rapid cooling to 0 K from each temperature. The energy of each phase except stishovite increases monotonically with an increasing temperature without any unreasonable decrease and shows an abrupt change with melting. Stishovite has much higher energy than other polymorphs and transforms to an unknown (amorphouslike) structure during heating according to our potential. However, the transformed structure remains as the highest energy structure among the SiO_2 polymorphs considered. The calculated specific heat of α-quartz is 76 J/mole K at 300 K, while the experimental data [133] is 50–75 J/mole K in a temperature range of 300–800 K. The volumetric thermal expansion behavior of α-quartz according to the present potential is somewhat complicated. The volume decreases with an increasing temperature at $-8.6 \times 10^{-6}\,K^{-1}$ in the range of 100–1000 K and then slightly increases at $8.4 \times 10^{-7}\,K^{-1}$, while a monotonic increase is observed experimentally with a volume expansion coefficient of $3.5 \times 10^{-5}\,K^{-1}$ at 300 K [133]. When rapidly cooled to 0 K from each heating temperature, the energy and structure of some phases are not completely recovered. We believe that this is because the structures of SiO_2 polymorphs are quite complicated and distorted, and also because the mutual energy differences among the polymorphs are small (see Table XI). It should be also mentioned that SiO_2 is mostly grown and used in an amorphous state. Several structures of amorphous SiO_2 can be generated by rapidly cooling liquid samples. To obtain a representative amorphous SiO_2 structure, several samples were generated by cooling to 300 K and annealing

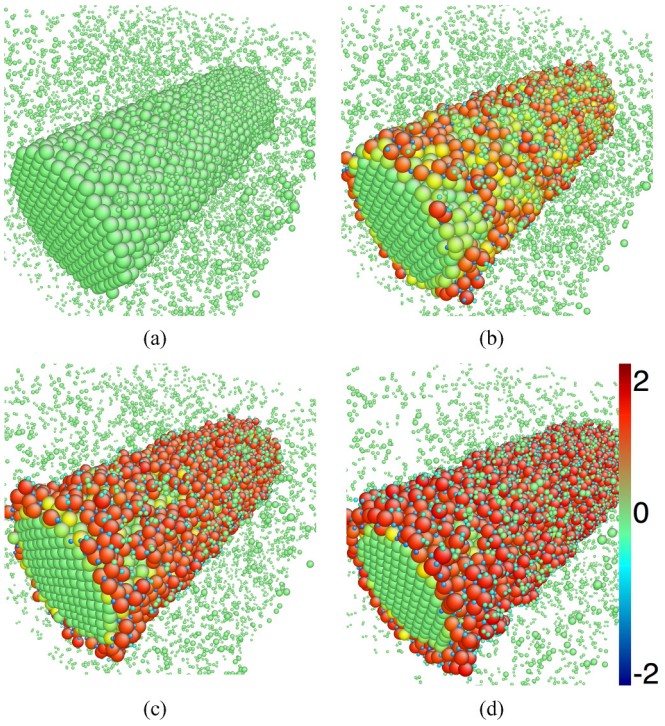

FIG. 8. Snapshots of molecular dynamics simulation for an oxidation reaction of a Ti nanowire, (a) initial state, after (b) 100, (c) 200, and (d) 500 picoseconds at 300 K, with coloring by charge state. Small spheres represent O atoms, while large spheres represent Ti atoms.

for 300 picoseconds at the same temperature with an N-P-T ensemble. Out of the generated amorphous structures, the structure with the closest peak positions in radial distribution functions for Si-Si (3.12 Å), Si-O (1.62 Å), and O-O (2.65 Å) bonding to experimental information [134] is selected as the representative amorphous structure. The energy of the amorphous SiO_2 is calculated to be higher than that of α-quartz by 0.33 eV/SiO_2 and the density of amorphous SiO_2 is calculated to be 2.00 g/cm^3 (experimental value is 2.20 g/cm^3) [134]. Corresponding values by COMB2 [42] are 0.13 eV/SiO_2 and 2.458 g/cm^3. The ratio between the density of amorphous SiO_2 and α-quartz according to the present potential is 0.83, which is in a good agreement with experimental value, 0.83 [134].

Finally, as a means to demonstrate the power of the variable charge potential, the oxidation reaction of Ti nanowire and the Si/SiO_2 (α-quartz) interface structure are simulated, as shown in Figs. 8–10. Here, the color represents the charge state. Figure 9 compares the oxidation rate on two Ti nanowires with different surface planes $(10\bar{1}0)$ or $(11\bar{2}0)$. It is shown that the nanowire with $(11\bar{2}0)$ surface planes reacts faster with oxygen molecules at least at the beginning stage of the oxidation reaction. The surface energy of the $(10\bar{1}0)$ and the $(11\bar{2}0)$ planes is calculated [68] to be 2145 and 2352 erg/cm^2, respectively. The present results show that the surface with higher energy may react faster than the surfaces with relative lower energy, but detailed analysis is left as a future study. One can expect that the effects of surface orientation, existence of grain boundary, alloying elements on the oxidation behavior

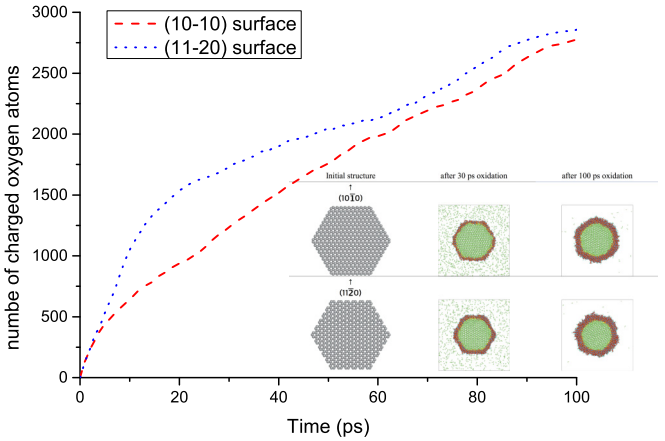

FIG. 9. Number of charged oxygen atoms along oxidation time for two Ti nanowires with different surface planes, $(10\bar{1}0)$ and $(11\bar{2}0)$. The oxygen atoms negatively charged more than $-0.5e$ are counted as charged oxygen atoms. The surface energy of the $(10\bar{1}0)$ and $(11\bar{2}0)$ plane is calculated to be 2145 and 2352 erg/cm^2, respectively [68].

of metals, as well as the interfacial structure of heterogeneous systems can be investigated using the variable charge potential. The energy of Si/SiO_2 interface (a) and interface (c) in Fig. 10 is calculated to be 3.12 and 2.84 J/m^2, respectively, but these are not systematically sought minimum energy surfaces between Si and α-quartz.

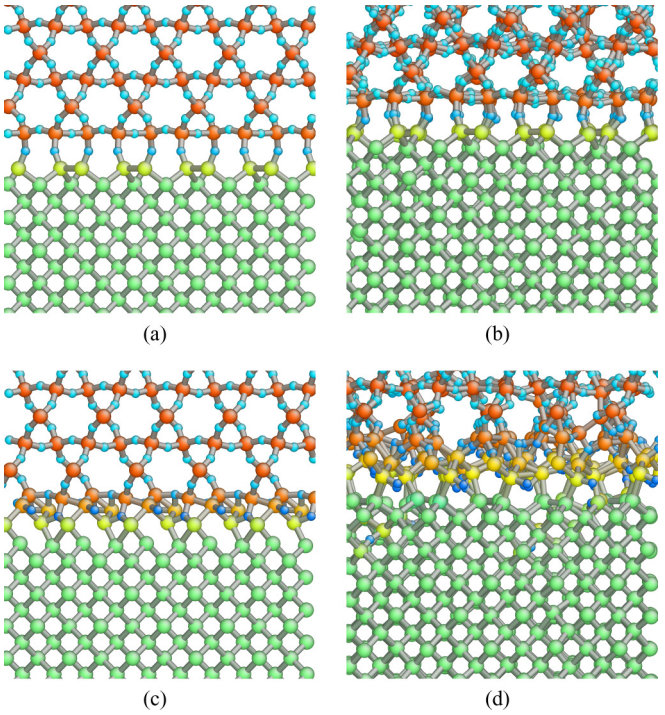

FIG. 10. Simulated interface structure between Si(010) and α-quartz SiO_2(010), (a) relaxed at 0 K and (b) annealed at 300 K during 100 picoseconds. Another configuration with a slightly lower interfacial energy obtained by shifting α-quartz layer, (c) relaxed at 0 K and (d) annealed at 300 K during 100 picoseconds. The color represents the charge state, with the same scale bar as in Fig. 8. The calculated interfacial energy of interface (a) is 3.12 J/m^2, while that of interface (c) is 2.84 J/m^2.

IV. CONCLUSION

We present an interatomic potential model that describes metallic, covalent, and ionic bonding simultaneously in a form that combines the existing 2NNMEAM and the concept of Qeq. We complete an electrostatic energy model by newly developing a mathematical form for the atomic energy and combining selected computational techniques for energy minimization, summation of Coulomb interaction, and charge representation in an optimized way. We pay special attention to the removal of already reported shortcomings in the original Qeq and also to computational efficiency. The potentials for the Ti-O and Si-O binary systems reproduce the structural, elastic, and thermodynamic properties of a wide range of titanium oxides and silicon oxides, in reasonable agreement with experiments and DFT calculations, and perform reasonably also for defect properties and at high pressures and temperatures. The proposed 2NNMEAM + Qeq potential model will be a good companion interatomic potential model to existing COMB and ReaxFF and is expected to perform better for multicomponent metallic oxide systems.

ACKNOWLEDGMENT

This research was supported by the Industrial Strategic Technology Development Program (Grant No. 10041589) funded by the Ministry of Knowledge Economy (MKE, Korea).

APPENDIX: DETAILS IN USING THE SPLIT-CHARGE MODEL

If using the split-charge model, the total electrostatic energy Eq. (13) can be rewritten by substituting Eq. (17),

$$E_{\text{total}}^{\text{ES}} = \sum_{i}^{N}\left[\sum_{j}^{R_{ij}<R_{ij}^{\text{bond}}} \bar{q}_{ji}\right]\chi_i + \frac{1}{2}\sum_{i,j}^{N}\left[\sum_{k}^{R_{ik}<R_{ik}^{\text{bond}}} \bar{q}_{ki}\right] \times \left[\sum_{l}^{R_{lj}<R_{lj}^{\text{bond}}} \bar{q}_{lj}\right] J_{ij}. \tag{A1}$$

For a given configuration of atoms, we can define all the split charges by pairing atoms within the cutoff distance, R_{ij}^{bond}, avoiding any duplication from the opposite direction of charge flow. For a system with a total number of bonds M, we can generalize Eq. (A1) using index of bonds ab or cd as

$$E_{\text{total}}^{\text{ES}} = \sum_{ab}^{M}\bar{q}_{ab}(\chi_b - \chi_a) + \frac{1}{2}\sum_{ab,cd}^{M}\bar{q}_{ab}\bar{q}_{cd}[(J_{ac} - J_{ad}) - (J_{bc} - J_{bd})]. \tag{A2}$$

The coefficient of the first-order term in Eq. (A2) can be determined by combining $\bar{q}_{ab}$ and $\bar{q}_{ba}$ in Eq. (A1). Similarly, the coefficient of the second-order term in Eq. (A2) is determined by assembling possible combinations of the bond index. We can construct a matrix equation based on Eq. (A2),

$$E_{\text{total}}^{\text{ES}} = \bar{\mathbf{q}}^{\mathbf{T}}\mathbf{b} + \tfrac{1}{2}\bar{\mathbf{q}}^{\mathbf{T}}\mathbf{A}\bar{\mathbf{q}}, \tag{A3}$$

where the M dimensional column vectors $\bar{\mathbf{q}}$ and $\mathbf{b}$ are the set of split charges and coefficients of the first-order term, respectively, and the M by M symmetric matrix $\mathbf{A}$ contains coefficients of the second-order term. The total electrostatic energy can be minimized by solving the following linear equation:

$$\frac{\partial E_{\text{total}}^{\text{ES}}}{\partial \bar{\mathbf{q}}} = \mathbf{b} + \mathbf{A}\bar{\mathbf{q}} = 0 \tag{A4}$$

using the CGM.

In addition to the concept of the split charge, Nistor *et al.* [74] also introduce an additional term to the electrostatic energy using a new binary parameter κ_{ij},

$$E_{\text{total}}^{\text{ES}} = \sum_{i}^{N} q_i\chi_i + \frac{1}{2}\sum_{i,j}^{N} q_i q_j J_{ij} + \sum_{ij}^{M}\bar{q}_{ij}^2\kappa_{ij}, \tag{A5}$$

where κ_{ij} can be interpreted as a bond hardness, in order to improve accuracy of predicting Muliken charges. However, Nistor *et al.* [75] and Mathieu [135] point out that it can lead to an abrupt change in energy and atomic charges during bond breaking, particularly when interatomic distances are near R^{bond}. Mathieu proposed an idea where the split charge can vanish smoothly as interatomic distances get close to a threshold value (bond breaking limit) by modifying bond hardness κ_{ij} to be dependent on interatomic distances. We, however, determine that this bond hardness term is not essential because the analogous physical meaning is sufficiently included in the presently modified electrostatic energy expression. Moreover, the expense to avoid the discontinuous changes of charge and energy during bond breaking is not trivial. Therefore, in this study, we do not include the bond hardness term but just take the concept of the split charge.

[1] L. V. Woodcock, Chem. Phys. Lett. **10**, 257 (1971).
[2] A. Rahman, R. H. Fowler, and A. H. Narten, J. Chem. Phys. **57**, 3010 (1972).
[3] W. R. Busing, J. Chem. Phys. **57**, 3008 (1972).
[4] S. Tsuneyuki, M. Tsukada, H. Aoki, and Y. Matsui, Phys. Rev. Lett. **61**, 869 (1988).
[5] N. R. Keskar and J. R. Chelikowsky, Phys. Rev. B **46**, 1 (1992).
[6] B. W. H. van Beest, G. J. Kramer, and R. A. van Santen, Phys. Rev. Lett. **64**, 1955 (1990).
[7] G. V. Lewis and C. R. A. Catlow, J. Phys. C Solid State Phys. **18**, 1149 (1985).
[8] P. Tangney and S. Scandolo, J. Chem. Phys. **117**, 8898 (2002).
[9] M. S. Daw and M. I. Baskes, Phys. Rev. Lett. **50**, 1285 (1983).
[10] M. S. Daw and M. I. Baskes, Phys. Rev. B **29**, 6443 (1984).
[11] M. I. Baskes, Phys. Rev. Lett. **59**, 2666 (1987).
[12] M. I. Baskes, J. S. Nelson, and A. F. Wright, Phys. Rev. B **40**, 6085 (1989).
[13] M. I. Baskes, Phys. Rev. B **46**, 2727 (1992).
[14] B.-J. Lee and M. I. Baskes, Phys. Rev. B **62**, 8564 (2000).

[15] See https://cmse.postech.ac.kr/home_2nnmeam.
[16] J. H. Rose, J. Ferrante, and J. R. Smith, Phys. Rev. Lett. **47**, 675 (1981).
[17] J. R. Smith, J. Ferrante, and J. H. Rose, Phys. Rev. B **25**, 1419 (1982).
[18] J. H. Rose, J. R. Smith, and J. Ferrante, Phys. Rev. B **28**, 1835 (1983).
[19] J. H. Rose, J. R. Smith, F. Guinea, and J. Ferrante, Phys. Rev. B **29**, 2963 (1984).
[20] G. C. Abell, Phys. Rev. B **31**, 6184 (1985).
[21] J. Tersoff, Phys. Rev. Lett. **56**, 632 (1986).
[22] J. Tersoff, Phys. Rev. B **37**, 6991 (1988).
[23] D. W. Brenner, Phys. Rev. B **42**, 9458 (1990).
[24] D. W. Brenner, O. A. Shenderova, J. A. Harrison, S. J. Stuart, B. Ni, and S. B. Sinnott, J. Phys.: Condens. Matter **14**, 783 (2002).
[25] S. J. Stuart, A. B. Tutein, and J. A. Harrison, J. Chem. Phys. **112**, 6472 (2000).
[26] S. Nouranian, M. A. Tschopp, S. R. Gwaltney, M. I. Baskes, and M. F. Horstemeyer, Phys. Chem. Chem. Phys. **16**, 6233 (2014).
[27] J. Yu, S. B. Sinnott, and S. R. Phillpot, Philos. Mag. Lett. **89**, 136 (2009).
[28] T. Liang, S. R. Phillpot, and S. B. Sinnott, Phys. Rev. B **79**, 245110 (2009).
[29] A. K. Rappe and W. A. Goddard III, J. Phys. Chem. **95**, 3358 (1991).
[30] E. Demiralp, T. Çağin, and W. A. Goddard III, Phys. Rev. Lett. **82**, 1708 (1999).
[31] V. Swamy and J. D. Gale, Phys. Rev. B **62**, 5406 (2000).
[32] V. Swamy, J. D. Gale, and L. S. Dubrovinsky, J. Phys. Chem. Solids **62**, 887 (2001).
[33] F. H. Streitz and J. W. Mintmire, Phys. Rev. B **50**, 11996 (1994).
[34] X. W. Zhou, H. N. G. Wadley, J.-S. Filhol, and M. N. Neurock, Phys. Rev. B **69**, 035402 (2004).
[35] X. W. Zhou and H. N. G. Wadley, J. Phys.: Condens. Matter **17**, 3619 (2005).
[36] X. W. Zhou and F. P. Doty, Phys. Rev. B **78**, 224307 (2008).
[37] X. W. Zhou, F. P. Doty, and P. Yang, Comput. Mater. Sci. **50**, 2470 (2011).
[38] I. Lazić and B. J. Thijsse, Comput. Mater. Sci. **53**, 483 (2012).
[39] F. Kong, H. Zhang, R. C. Longo, B. Lee, D. H. Yeon, J. Yoon, J. H. Park, S. G. Doo, and K. Cho, Comput. Mater. Sci. **112**, 193 (2016).
[40] A. Yasukawa, JSME Int. J. Ser. A **39**, 313 (1996).
[41] J. Yu, S. B. Sinnott, and S. R. Phillpot, Phys. Rev. B **75**, 085311 (2007).
[42] T.-R. Shan, B. D. Devine, J. M. Hawkins, A. Asthagiri, S. R. Phillpot, and S. B. Sinnott, Phys. Rev. B **82**, 235302 (2010).
[43] T.-R. Shan, B. D. Devine, T. W. Kemper, S. B. Sinnott, and S. R. Phillpot, Phys. Rev. B **81**, 125328 (2010).
[44] T.-R. Shan, B. D. Devine, S. R. Phillpot, and S. B. Sinnott, Phys. Rev. B **83**, 115327 (2011).
[45] B. Devine, T.-R. Shan, Y.-T. Cheng, A. J. H. McGaughey, M. Lee, S. R. Phillpot, and S. B. Sinnott, Phys. Rev. B **84**, 125308 (2011).
[46] Y.-T. Cheng, T.-R. Shan, B. Devine, D. Lee, T. Liang, B. B. Hinojosa, S. R. Phillpot, A. Asthagiri, and S. B. Sinnott, Surf. Sci. **606**, 1280 (2012).
[47] T. Liang, B. Devine, S. R. Phillpot, and S. B. Sinnott, J. Phys. Chem. A **116**, 7976 (2012).
[48] Y. Li, T.-R. Shan, T. Liang, S. B. Sinnott, and S. R. Phillpot, J. Phys.: Condens. Matter **24**, 235403 (2012).
[49] Y.-T. Cheng, T.-R. Shan, T. Liang, R. K. Behera, S. R. Phillpot, and S. B. Sinnott, J. Phys.: Condens. Matter **26**, 315007 (2014).
[50] T. Liang, Y. K. Shin, Y.-T. Cheng, D. E. Yilmaz, K. G. Vishnu, O. Verners, C. Zou, S. R. Phillpot, S. B. Sinnott, and A. C. T. van Duin, Annu. Rev. Mater. Res. **43**, 109 (2013).
[51] T. Liang, T.-R. Shan, Y.-T. Cheng, B. D. Devine, M. Noordhoek, Y. Li, Z. Lu, S. R. Phillpot, and S. B. Sinnott, Mater. Sci. Eng. R **74**, 255 (2013).
[52] A. C. T. van Duin, S. Dasgupta, F. Lorant, and W. A. Goddard III, J. Phys. Chem. A **105**, 9396 (2001).
[53] K. Chenoweth, A. C. T. van Duin, and W. A. Goddard III, J. Phys. Chem. A **112**, 1040 (2008).
[54] D. Chakraborty, R. P. Muller, S. Dasgupta, and W. A. Goddard III, J. Phys. Chem. A **104**, 2261 (2000).
[55] J. E. Mueller, A. C. T. van Duin, and W. A. Goddard III, J. Phys. Chem. C **114**, 4939 (2010).
[56] J. E. Mueller, A. C. T. van Duin, and W. A. Goddard III, J. Phys. Chem. C **114**, 5675 (2010).
[57] B. Liu, M. T. Lusk, and J. F. Ely, Surf. Sci. **606**, 615 (2012).
[58] L. Meng, Q. Sun, J. Wang, and F. Ding, J. Phys. Chem. C **116**, 6097 (2012).
[59] A. C. T. van Duin, A. Strachan, S. Stewman, Q. Zhang, X. Xu, and W. A. Goddard III, J. Phys. Chem. A **107**, 3803 (2003).
[60] F. Fan, S. Huang, H. Yang, M. Raju, D. Datta, V. B. Shenoy, A. C. T. van Duin, S. Zhang, and T. Zhu, Model. Simul. Mater. Sci. Eng. **21**, 074002 (2013).
[61] S. Naserifar, L. Liu, W. A. Goddard III, T. T. Tsotsis, and M. Sahimi, J. Phys. Chem. C **117**, 3308 (2013).
[62] S. Naserifar, W. A. Goddard III, L. Liu, T. T. Tsotsis, and M. Sahimi, J. Phys. Chem. C **117**, 3320 (2013).
[63] Q. Zhang, T. Çağın, A. van Duin, W. A. Goddard III, Y. Qi, and L. G. Hector, Jr., Phys. Rev. B **69**, 045423 (2004).
[64] S. Blackwell, R. Smith, S. D. Kenny, J. M. Walls, and C. F. Sanz-Navarro, J. Phys.: Condens. Matter **25**, 135002 (2013).
[65] S.-Y. Kim, N. Kumar, P. Persson, J. Sofo, A. C. T. van Duin, and J. D. Kubicki, Langmuir **29**, 7838 (2013).
[66] B.-J. Lee, M. I. Baskes, H. Kim, and Y. K. Cho, Phys. Rev. B **64**, 184102 (2001).
[67] B.-J. Lee, J.-H. Shim, and M. I. Baskes, Phys. Rev. B **68**, 144112 (2003).
[68] Y.-M. Kim, B.-J. Lee, and M. I. Baskes, Phys. Rev. B **74**, 014101 (2006).
[69] Y.-M. Kim, N. J. Kim, and B.-J. Lee, Calphad **33**, 650 (2009).
[70] Y.-M. Kim, Y.-H. Shin, and B.-J. Lee, Acta Mater. **57**, 474 (2009).
[71] B.-J. Lee and J. W. Lee, Calphad **29**, 7 (2005).
[72] B.-J. Lee, Calphad **31**, 95 (2007).
[73] E. H. Kim, Y.-H. Shin, and B.-J. Lee, Calphad **32**, 34 (2008).
[74] B.-J. Lee, W.-S. Ko, H.-K. Kim, and E.-H. Kim, Calphad **34**, 510 (2010).
[75] R. A. Nistor, J. G. Polihronov, M. H. Müser, and N. J. Mosey, J. Chem. Phys. **125**, 094108 (2006).
[76] C. E. Wilmer, K. C. Kim, and R. Q. Snurr, J. Phys. Chem. Lett. **3**, 2506 (2012).
[77] P. Vinet, J. Ferrante, J. R. Smith, and J. H. Rose, J. Phys. C: Solid State Phys. **19**, L467 (1986).

[78] J. R. Smith, H. Schlosser, W. Leaf, J. Ferrante, and J. H. Rose, Phys. Rev. A **39**, 514 (1989).

[79] J. Ferrante, H. Schlosser, and J. R. Smith, Phys. Rev. A **43**, 3487 (1991).

[80] D. E. Parry, Surf. Sci. **49**, 433 (1975).

[81] D. Wolf, P. Keblinski, S. R. Phillpot, and J. Eggebrecht, J. Chem. Phys. **110**, 8254 (1999).

[82] S. W. Rick, S. J. Stuart, and B. J. Berne, J. Chem. Phys. **101**, 6141 (1994).

[83] D. J. Keffer and J. W. Mintmire, Int. J. Quantum Chem. **80**, 733 (2000).

[84] G. Herzberg, *Molecular Spectra and Molecular Structure III. Electronic Spectra and Electronic Structure of Polyatomic Molecules* (D. Van Nostrand Company, Ltd., Princeton, NJ, 1966).

[85] S. C. Abrahams and J. L. Bernstein, J. Chem. Phys. **55**, 3206 (1971).

[86] D. G. Isaak, J. D. Carnes, O. L. Anderson, H. Cynn, and E. Hake, Phys. Chem. Miner. **26**, 31 (1998).

[87] J. K. Burdett, T. Hughbanks, G. J. Miller, J. W. Richardson, Jr., and J. V. Smith, J. Am. Chem. Soc. **109**, 3639 (1987).

[88] V. Swamy and L. S. Dubrovinsky, J. Phys. Chem. Solids **62**, 673 (2001).

[89] E. P. Meagher and G. A. Lager, Can. Mineral. **17**, 77 (1979).

[90] W. Luo, S. F. Yang, Z. C. Wang, Y. Wang, R. Ahuja, B. Johansson, J. Liu, and G. T. Zou, Solid State Commun. **133**, 49 (2005).

[91] R. Marchand, L. Brohan, and M. Tournoux, Mater. Res. Bull. **15**, 1129 (1980).

[92] M. Latroche, L. Brohan, R. Marchand, and M. Tournoux, J. Solid State Chem. **81**, 78 (1989).

[93] J. Akimoto, Y. Gotoh, Y. Oosawa, N. Nonose, T. Kumagai, K. Aoki, and H. Takei, J. Solid State Chem. **113**, 27 (1994).

[94] I. E. Grey, C. Li, I. C. Madsen, and G. Braunshausen, Mater. Res. Bull. **23**, 743 (1988).

[95] J. S. Olsen, L. Gerward, and J. Z. Jiang, J. Phys. Chem. Solids **60**, 229 (1999).

[96] H. Sato, S. Endo, M. Sugiyama, T. Kikegawa, O. Shimomura, and K. Kusaba, Science **251**, 786 (1991).

[97] L. S. Dubrovinsky, N. A. Dubrovinskaia, V. Swamy, J. Muscat, N. M. Harrison, R. Ahuja, B. Holm, and B. Johansson, Nature (London) **410**, 653 (2001).

[98] Y. Le Page and P. Strobel, J. Solid State Chem. **47**, 6 (1983).

[99] M. Marezio and P. D. Dernier, J. Solid State Chem. **3**, 340 (1971).

[100] I. E. Grey, C. Li, and I. C. Madsen, J. Solid State Chem. **113**, 62 (1994).

[101] S.-H. Hong and S. Åsbrink, Acta Crystallogr., Sect. B: Struct. Sci., Cryst. Eng. Mater. **38**, 2570 (1982).

[102] C. E. Rice and W. R. Robinson, J. Solid State Chem. **21**, 145 (1977).

[103] D. Watanabe, J. R. Castles, A. Jostsons, and A. S. Malin, Acta Crystallogr. **23**, 307 (1967).

[104] Y. Syono, T. Goto, J. Nakai, Y. Nakagawa, and H. Iwasaki, J. Phys. Soc. Jpn. **37**, 442 (1974).

[105] A. Jain, S. P. Ong, G. Hautier, W. Chen, W. D. Richards, S. Dacek, S. Cholia, D. Gunter, D. Skinner, G. Ceder, and K. A. Persson, APL Mater. **1**, 011002 (2013).

[106] B.-J. Lee and N. Saunders, Z. Metallkd. **88**, 152 (1997).

[107] A. Navrotsky and O. J. Kleppa, J. Am. Ceram. Soc. **50**, 626 (1967).

[108] A. Hallil, E. Amzallag, S. Landron, and R. Tétot, Surf. Sci. **605**, 738 (2011).

[109] S. K. Wallace and K. P. Mckenna, J. Phys. Chem. C **119**, 1913 (2015).

[110] M. Lazzeri, A. Vittadini, and A. Selloni, Phys. Rev. B **63**, 155409 (2001).

[111] J. He and S. B. Sinnott, J. Am. Ceram. Soc. **88**, 737 (2005).

[112] T. S. Bjørheim, A. Kuwabara, and T. Norby, J. Phys. Chem. C **117**, 5919 (2013).

[113] Y. Kudoh and H. Takeda, Physica B+C **139–140**, 333 (1986).

[114] T. Arlt, M. Bermejo, M. A. Blanco, L. Gerward, J. Z. Jiang, J. S. Olsen, and J. M. Recio, Phys. Rev. B **61**, 14414 (2000).

[115] L. Levien, C. T. Prewitt, and D. J. Weidner, Am. Mineral. **65**, 920 (1980).

[116] A. F. Wright and M. S. Lehmann, J. Solid State Chem. **36**, 371 (1981).

[117] W. A. Dollase, Acta Crystallogr. **23**, 617 (1967).

[118] R. T. Downs and D. C. Palmer, Am. Mineral. **79**, 9 (1994).

[119] T. F. W. Barth, Am. J. Sci. **24**, 97 (1932).

[120] L. Levien and C. T. Prewitt, Am. Mineral. **66**, 324 (1981).

[121] J. Shropshire, P. P. Keat, and P. A. Vaughan, Z Kristalllogr. **112**, 409 (1959).

[122] N. L. Ross, J. Shu, R. M. Hazen, and T. Gasparik, Am. Mineral. **75**, 739 (1990).

[123] T. Demuth, Y. Jeanvoine, J. Hafner, and J. G. Ángyán, J. Phys.: Condens. Matter **11**, 3833 (1999).

[124] C.-L. Kuo and P. Clancy, Model. Simul. Mater. Sci. Eng. **13**, 1309 (2005).

[125] H. J. McSkimin, P. Andreatch, Jr., and R. N. Thurston, J. Appl. Phys. **36**, 1624 (1965).

[126] A. Yeganeh-Haeri, D. J. Weidner, and J. B. Parise, Science **257**, 650 (1992).

[127] H. Kimizuka, H. Kaburaki, and Y. Kogure, Phys. Rev. Lett. **84**, 5548 (2000).

[128] P. Richet, Y. Bottinga, L. Denielou, J. P. Petiet, and C. Tequi, Geochim. Cosmochim. Acta **46**, 2639 (1982).

[129] *CRC Handbook of Chemistry and Physics*, 64th ed. (CRC, Boca Raton, FL, 1983).

[130] O. I. Malyi, V. V. Kulish, and C. Persson, RCS Adv. **4**, 55599 (2014).

[131] G. Roma, Y. Limoge, and S. Baroni, Phys. Rev. Lett. **86**, 4564 (2001).

[132] U. Diebold, Surf. Sci. Rep. **48**, 53 (2003).

[133] M. A. Carpenter, E. K. H. Salje, A. Graeme-Barber, B. Wruck, M. T. Dove, and K. S. Knight, Am. Mineral. **83**, 2 (1998).

[134] R. L. Mozzi and B. E. Warren, J. Appl. Crystallogr. **2**, 164 (1969).

[135] D. Mathieu, J. Chem. Phys. **127**, 224103 (2007).